PHOTONIC CRYSTALS

PHOTONIC BAND GAP MATERIALS

Photonic crystals are a novel class of artificially fabricated periodic structures that can control, manipulate and guide the propagation of electromagnetic waves in ways not possible with conventional materials. Photonic crystals can inhibit the propagation of light, allow it only in certain frequency regions, or localize light in specific spatial regions. Photonic crystals can be synthesized in one, two, and three dimensions (*1-D*, *2-D*, and *3-D*) with dielectric or/and metallic materials.

The concept of photonic band structure is analogous to the well-established concept of electronic band structure. Just as electron waves, traveling in the periodic potential of a crystal, are arranged into energy bands separated by band gaps, we expect the analogous phenomenon to occur when electromagnetic (*EM*) waves propagate in a medium where the dielectric constant varies periodically in space. There is a special interest in structures that can produce a forbidden frequency gap in which all propagating states are prohibited: such materials are called photonic band gap materials and are the topic of intensive studies by many groups theoretically and experimentally (1–4).

Photonic band gaps may have a profound impact on many areas in basic and applied physics. Because of the absence of optical modes in the gap, spontaneous emission is suppressed for photons with frequencies in the forbidden region. It has been suggested that, by tuning the photonic band gap to overlap with the electronic band edge, electron–hole recombination can be controlled in a photonic band gap material, leading to enhanced efficiency and reduced noise in the operation of optoelectronic devices (5) and lasing structures. The suppression of spontaneous emission can be used to prolong the lifetimes of selected chemical species in catalytic processes (6–8). Photonic band gap materials can also find applications in frequency-selective mirrors, bandpass filters, and resonators. Besides applications at various frequencies in the electromagnetic spectrum, there is much interest in the phenomenon of localization of EM waves by the introduction of defects and disorder in a photonic band gap material (<xref target="W4410-bib-0009 W4410-bib-0010 W4410-bib-0011 W4410-bib-0012" style="unformatted"/>). This will be an ideal realization of the phenomenon of localization uncomplicated by many-body effects present in the case of electron localization. Another interesting effect is that zero-point fluctuations, which are present even in vacuum, are absent for frequencies within a photonic gap.

Over the past decade, there has been rapid development in this field in the fabrication of photonic band gap materials. Unlike the case of electron waves, which usually have wavelengths on the atomic scale, the wavelengths of electromagnetic waves of interest are several orders of magnitude larger, varying between hundreds of nanometers for visible light to meters and centimeters for radio and microwaves. While the periodic lattice for electron waves is constrained by the crystal structure, the periodic dielectric structures for photonic band gap materials are artificial structures that can be designed and fabricated to provide a desired electromagnetic response. Therefore, there is much interest in theoretical calculations for these systems, and advances in the field have been characterized by a close collaboration between theorists and experimentalists. The absence of the photon-photon interaction makes photonic crystals an ideal testing ground for theoretical simulation, bypassing the complications with electron-electron interactions inherent in the analogous electronic case.

One-dimensional photonic crystals have been well known for several decades as the distributed Bragg reflector (DBR), and they are the basis of many devices, such as dielectric mirrors, Fabry-Perot filters, and distributed feedback lasers (13–15). A 1-D photonic crystal (PC) is shown in Fig. 1(a). A typical example of a 1-D PC with periodicity a, is a superlattice of alumina layers (with dielectric constant, ε = 9.61) and air layers (?=1). We consider alumina thicknesses of 0.4375 mm and air layers with thickness of 1.3125 mm, designed for millimeter region of the electromagnetic spectrum. Simulations for waves incident on the structure at three different incident angles (0°, 30°, and 60°) are shown in Fig. 1(b) and 1(c). For normal incidence (solid lines in Fig. 1), there is a drop of the transmission from about 36 to 77 GHz. The transmission at the center of the gap is almost five orders (almost −50 dB) of magnitude less than the incident wave. Calculations are based on the real space transfer matrix method described later. The gap results from the multiple interference of waves, from the different layers of the structure, and there is destructive interference of transmitted waves within the band gap region. As is well-known for geometrical optics the wavelength of the gap appears when the wavelength λ is $2n_{eff}a$ where n_{eff} is the effective refractive index of the multilayer. We expect the gap to disappear for other incident angles. Indeed, by increasing the incident angle, the gap increases for the polarization with the electric field out of the plane of incidence [see Fig. 1(b)], but the gap tends to disappear for the wave polarized in the plane of incidence [see Fig. 1(c)].

A physical realization of a 2-D photonic crystal is obtained using infinitely long cylinders arranged in the 2-D triangular lattice (1–4) with the cross section of this structure shown in Fig. 2(a). The cylinders may be composed of air residing in a dielectric background or of dielectric material residing in an air background. The transmission for EM waves with incident k vector in the x,z plane is shown in Fig. 2. We use air cylinders with radius 0.805 mm surrounded by a dielectric with ε = 12.25 (the dielectric constant of GaAs); the distance between the center of the cylinders is 1.75 mm, and the total thickness of the system along the z direction is 9.1 mm. For waves with E field parallel to the cylinders [Fig. 2(b)], there is a small gap at around 48 GHz and a much wider gap at around 80 GHz. As the incident angle increases and the k vector is perpendicular to the axis of the cylinders, the second gap moves to smaller frequencies. For the polarization with the E field in the x,z plane [Fig. 2(c)], there is a gap at around 70 GHz for all the angles and for k vectors perpendicular to the axis of the cylinders. For both polarizations and for k vectors in the x,z plane, there is a gap from 70 to 80 GHz.

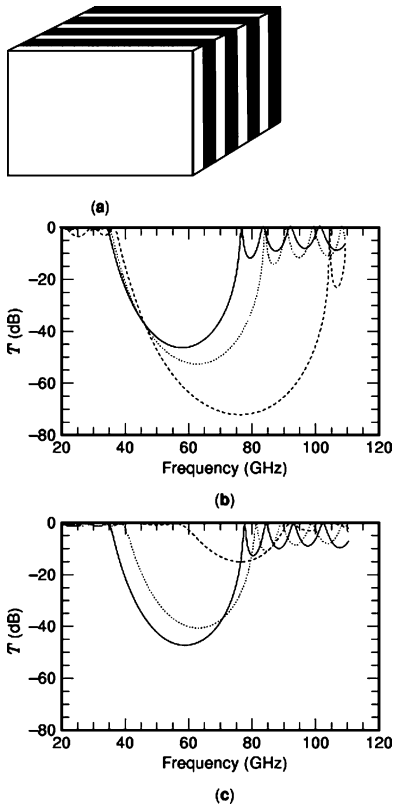

Figure 1. The transmission for EM waves propagating in a one-dimensional photonic crystal [see panel (a)] for incident angle of 0°, 30°, and 60° (solid, dotted, and dashed lines, respectively). The incident k vector is always in the x,z plane. Panels (b) and (c) correspond to E fields parallel to the y axis and in the x,z plane, respectively.

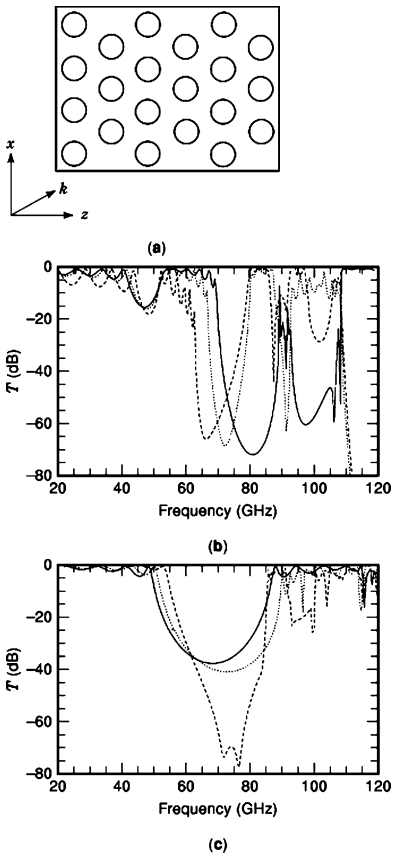

Figure 2. The transmission for EM waves propagating in a two-dimensional photonic crystal. The cross section of the structure is shown in panel (a). The incident angle is 0°, 30°, and 60° (solid, dotted, and dashed lines, respectively). The incident k vector is always in the x,z plane. Panels (b) and (c) correspond to E fields parallel to the y axis and in the x,z plane, respectively.

This structure of the triangular lattice with air columns in a dielectric background is the only known 2-D PC that has a gap for both polarizations and has been used extensively for applications. As in the 1-D case, we expect that the gap will disappear as the k vector moves out of the x,z plane because the system is homogeneous along the y axis.

An important property of Maxwell's equations for dielectric systems in the absence of absorption or non-linearities is that the lattice spacing a can be scaled to any length scale by any factor γ, ($a\prime = \gamma a$), and the frequencies will scale as $f\prime = f/\gamma$ [3]. Although we have described the behavior of photonic crystals at millimeter wave frequencies, exactly the same electromagnetic response will occur when the structure is created at optical length scales. This scaling behavior allows photonic crystal structures to be designed, synthesized and measured at much more convenient microwave/millimeter wave frequencies to understand the behavior of the same photonic crystals at optical length scales.

It is clear that we need a 3-D structure with periodicity along three directions in order to have a complete photonic band gap where transmission of waves is forbidden for all polarizations and all the incident directions in a certain frequency range (the band gap). Intense research in the beginning of the 1990s described periodic structures a photonic band gaps (*PBG*) (<xref target="W4410-bib-0001 W4410-bib-0002 W4410-bib-0003 W4410-bib-0004 W4410-bib-0016 W4410-bib-0017" style="unformatted"/>). In fact, the first 3-D photonic crystal built by Yablonovitch and Gmitter (18) did not have a complete PBG. This structure consisted of air spheres embedded in an Al_2O_3 material forming a face-centered-cubic (*fcc*) lattice. We can visualize this crystal by placing the spheres at the edges and at the center of the faces of a cube. It was constructed by drilling hemispherical cavities on dielectric plates that were stacked together. The whole structure can be constructed by periodically displacing the cube into the space. In contrast to the transmission measurements, which showed a complete PBG for this structure because of a degeneracy of modes at a particular direction (19–21).

At this point, Ho, Chan, and Soukoulis (21,22) theoretically proved that the diamond structure consisting of air or dielectric spheres posesses a complete PBG. A diamond structure is similar to the fcc structure, but instead of placing one sphere in each fcc lattice point, we place one more sphere in each lattice point displaced parallel to the body diagonal of the cube by one quarter of the length of the diagonal. The first photonic crystal with a complete PBG was built by Yablonovitch et al. (23). They devised an ingenious way of constructing a diamond lattice. They noted

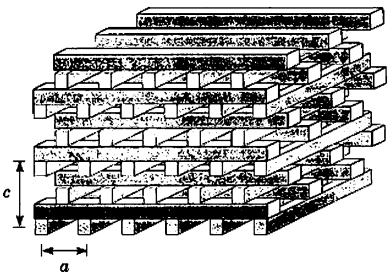

Figure 3. Layer-by-layer structure constructed by orderly stacking of dielectric rods. The periodicity is four layers in the stacking direction. Layers in the second neighbor layer are shifted by $a/2$ in the plane.

that the diamond lattice is a very open structure characterized by an open channel along the [110] directions. This structure was named the three cylinder structure, was can be constructed by drilling holes on the surface of a materials' slab. The holes form a triangular array. Three drilling operations are conducted through each hole, 35.26° off normal incidence and spread out 120° on the azimuth. The structure had a complete PBG centered at 14 GHz and the width of the forbidden gap was 19% of its center frequency.

Subsequently, the Iowa State group designed and fabricated the layer-by-layer structure shown in Fig. 3 (24). The structure is assembled by stacking layers consisting of parallel rods with a center-to-center separation of a. The rods are rotated by 90° in each successive layer. Starting at any reference layer, the rods of every second neighboring layer are parallel to the reference layer but shifted by a distance $0.5a$ perpendicular to the rod axes. This results in a stacking sequence that repeats every four layers. This lattice has face-centered-tetragonal (*fct*) lattice symmetry with a basis of two rods. This structure has a robust photonic band gap when both the filling ratio and the dielectric contrast meet certain requirements. The photonic band gap is not sensitive to the cross-sectional shape of the rods. Several different structures have been constructed with midgap frequencies at 13, 100, and 450 GHz using etching techniques and Al_2O_3 or Si as materials (25–30). The structure has been fabricated with a measured PBG at around 2 THz using laser-induced direct-write deposition from the gas phase (31).

Figures 4 and 5 show the transmission for a layer-by-layer structure with rods with a circular cross section; the radius of each rod is 20 μm, the in-plane separation of the rods is 160 μm, and the dielectric constant of the rods is 9.61. The crystal contains 12 layers of rods (3 unit cells). For propagation along the stacking direction (k parallel to the z axis), there is gap between 0.9 and 1.25 THz, and the transmitted intensity at the center of the gap is more than six orders of magnitude smaller than the incident intensity (−60 dB). By increasing the incident angle, the gap becomes smaller, and the transmission at the center of the gap increases, but there is a complete PBG for all the angles and polarizations between 0.9 and 1.05 THz.

By creating small distortions (or defects) in these photonic crystals, we can also create defect states inside the PBG, which give rise to sharp peaks of the transmission inside the PBG. This is analogous to donors or acceptors in

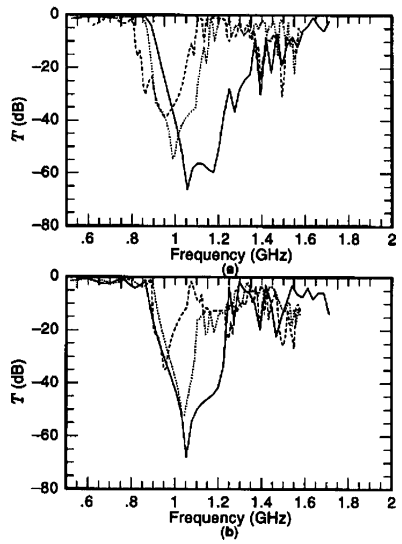

Figure 4. The transmission for EM waves propagating in a three-dimensional photonic crystal similar to the one shown in Fig. 3. The incident angle is 0°, 30°, and 60° (solid, dotted, and dashed lines, respectively). The incident k vector is always perpendicular to the y axis. Panels (a) and (b) correspond to *E fields parallel* to the y axis and in the x,z plane, respectively. The rods of the first layer are parallel to the y axis.

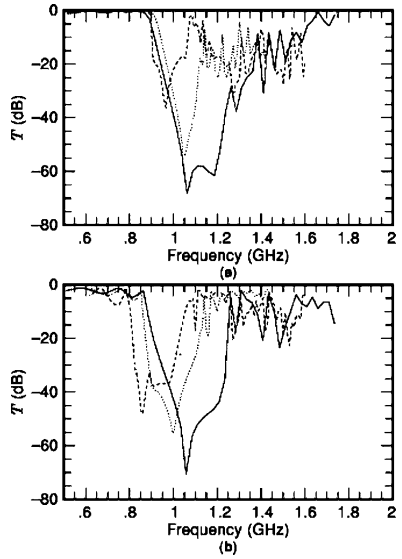

Figure 5. The same as in Fig. 4 except that the k vector is always perpendicular to the x axis.

semiconductors that introduce impurity states in the electronic energy gap. Such systems can be used as filters. Let us first study a 1-D photonic crystal with a defect (Fig. 6). The structure is the same as the one studied in Fig. 1, with one defect. In the third unit cell, the air slab has a thickness 0.8 times its original thickness, and the dielectric slab has a thickness 1.2 times its original thickness. As a result of that difference, the transmission for normal incidence has a peak inside the gap at 71 GHz (compare the solid lines in Figs. 1 and 6). However, when the incident angle increases, the transmission peak moves to higher frequencies and it appears at different frequencies for each polarization (com-

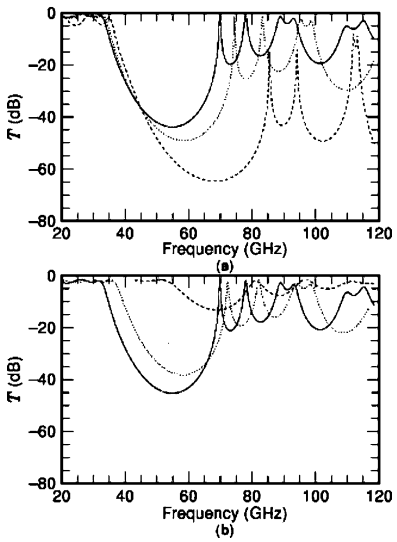

Figure 6. The transmission for EM waves propagating in a one-dimensional photonic crystal (similar to the one in Fig. 1) with a defect for incident angle of 0°, 30°, and 60° (solid, dotted, and dashed lines, respectively). The incident k vector is always in the x,z plane. Panels (a) and (b) correspond to E fields parallel to the y axis and in the x,z plane, respectively.

pare the different lines in Fig. 6). Even for the 30° angle, the transmission peak appears at 76 GHz (for E field perpendicular to the plane of incidence), 5 GHz higher than its value at normal incidence.

The strong dependence of the defect mode on the incident angle is again related to the fact that the 1-D photonic crystal is actually homogeneous along the x and y directions. It has been shown theoretically and experimentally that 3-D photonic crystals can solve this problem (29–34). For simplicity, we will illustrate this with a 2-D photonic crystal similar to the one in Fig. 2. Recall that 2-D photonic crystals suffer from the same disadvantage as the 1-D photonic crystals discussed in the previous paragraph. The reason for that problem is the homogeneity of the structure along the y axis [see Fig. 2(a)]. For that reason, we will show results only for k vectors in the x,z plane [see Fig. 2(a)] and for the E field parallel to the axis of the cylinders (y axis). The defect is introduced by decreasing the radius of one cylinder in the center of the structure. The distorted radius is 0.7 times its original value. For normal incidence (solid line in Fig. 7), there are three transmission peaks inside the gap, at 71, 76, and 78 GHz. For incident angle of 30°, the peaks remain at almost the same frequencies. The small changes in the frequency are actually an artifact of the calculations. We will return to this point when we discuss the computational method (transfer matrix method). We can tune the position of the transmission peak inside the gap, by changing the radius of the distorted cylinder. The flexibility in tuning defect modes makes photonic crystals a very attractive medium for the design of novel types of filters, couplers, laser microcavities, etc. (1–4).

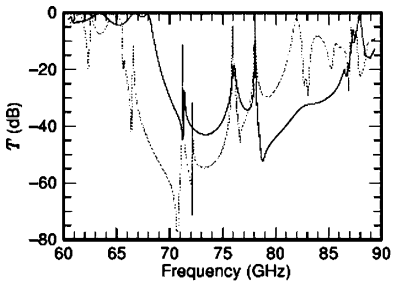

Figure 7. The transmission for EM waves propagating in a two-dimensional photonic crystal (similar to the one in Fig. 2) with a defect. The incident angle is 0° and 30° (solid and dotted, respectively). The incident k vector is always in the x,z plane. The E field is parallel to the y axis.

THEORETICAL METHODS

Plane Wave Method

To study the behavior of electromagnetic waves in photonic band gap crystals, we must solve Maxwell's equations for a media characterized by a spatially varying dielectric function $\varepsilon(\mathbf{r})$:

$$\nabla \cdot \mathbf{D} = 0 \tag{1}$$

$$\nabla \cdot \mathbf{H} = 0 \tag{2}$$

$$\nabla \times \mathbf{E} = i(\omega/c)\mathbf{H} \tag{3}$$

$$\nabla \times \mathbf{H} = -i(\omega/c)\mathbf{D} \tag{4}$$

$$\mathbf{D}(\mathbf{r}) = \epsilon(\mathbf{r})\mathbf{E}(\mathbf{r}) \tag{5}$$

These may be decoupled to generate an equation only in the magnetic field,

$$\nabla \times (\epsilon^{-1}(\mathbf{r})\nabla \times \mathbf{H}) = (\omega/c)^2\mathbf{H} \tag{6}$$

and

$$\nabla \times (\nabla \times \mathbf{E}) = (\omega/c)^2\epsilon(\mathbf{r})\mathbf{E} \tag{7}$$

At this point, we note that the vector nature of the wave equation is of crucial importance. Early attempts (35) at adopting the scalar wave approximation led to qualitatively wrong results. The simplest case happens when $\varepsilon(\mathbf{r})$ is a real and periodic function of r, and we assume that it is frequency-independent in the range of interest. We also assume the magnetic permeability μ is 1. In this case, the solution of the problem scales with the period of $\varepsilon(\mathbf{r})$. For example, reducing the size of the structure by a factor of two will not change the spectrum of electromagnetic modes other than scaling all frequencies up by a factor of two.

Because of the periodicity of the problem, we can make use of Bloch's theorem to expand the electric and magnetic fields in terms of Bloch waves:

$$\mathbf{H}(\mathbf{r}) = \sum_{\mathbf{K}} \mathbf{H}_{\mathbf{K}} \exp(i\mathbf{K} \cdot \mathbf{r}) \tag{8}$$

where $\mathbf{K} = \mathbf{k} + \mathbf{G}$. $\mathbf{k}$ is a vector in the Brillouin zone, and $\mathbf{G}$ is a reciprocal lattice vector. The solution for the magnetic

field has the form of an eigenvalue problem:

$$\sum_{\mathbf{K}} \mathbf{K} \times \epsilon^{-1}_{\mathbf{K},\mathbf{K}'} (\mathbf{K} \times \mathbf{H}_{\mathbf{K}'}) = -(\omega/c)^2 \mathbf{H}_{\mathbf{K}} \qquad (9)$$

The corresponding equation for the E field does not have the form of a simple eigenvalue problem because the dielectric function enters into the frequency-dependent right-hand side:

$$\mathbf{K} \times \mathbf{K} \times \mathbf{E}_{\mathbf{K}} = -(\omega/c)^2 \sum_{\mathbf{K}'} \epsilon_{\mathbf{K},\mathbf{K}'} \mathbf{E}_{\mathbf{K}'} \qquad (10)$$

Hence, we obtain photonic band structure by solving Eq. (9) for the magnetic fields.

Here $\varepsilon_{\mathbf{K},\mathbf{K}'} = \varepsilon(\mathbf{G} - \mathbf{G}')$ is the Fourier transform of the dielectric function. Dielectric functions with sharp spatial discontinuities require an infinite number of plane waves in the Fourier expansion. To avoid this problem, we smear out the interfaces of the dielectric objects in the unit cell. For example, for modeling a cylinder of radius a and dielectric ε, we employ the smeared dielectric function

$$\epsilon(\mathbf{r}) = 1 + (\epsilon - 1)/\{1 + \exp[(r - a)/w]\} \qquad (11)$$

where the width w of the interface is chosen as a small fraction of the radius a (≈ 0.01–$0.05\ a$). In practice, we incorporate the smearing and define the dielectric function $\varepsilon(r)$ over a grid in real space. The Fourier transform of the dielectric function in our finite plane wave basis set is computed to obtain $\varepsilon(\mathbf{G} - \mathbf{G}')$. The dielectric matrix in Fourier space is then inverted to obtain $\varepsilon^{-1}(\mathbf{G} - \mathbf{G}')$. This procedure yields much better convergence than the alternative method of determining $\varepsilon^{-1}(\mathbf{G} - \mathbf{G}')$.

The transverse components of the magnetic field are $h_{\mathbf{K},1}$, that is,

$$\mathbf{H}_{\mathbf{K}} = h_{\mathbf{K},1}\mathbf{e}_1 + h_{\mathbf{K},2}\mathbf{e}_2 \qquad (12)$$

where the unit vectors $\mathbf{e}_1$ and $\mathbf{e}_2$ form an orthogonal triad ($\mathbf{e}_1$, $\mathbf{e}_2$, $\mathbf{K}$). The solution in Eq. (9) for the magnetic field reduces to the eigenvalue problem:

$$\sum_{\mathbf{K}',\lambda'} M(\mathbf{K}, \lambda; \mathbf{K}', \lambda') h_{\mathbf{K}',\lambda'} = (\omega/c)^2 h_{\mathbf{K},\lambda} \qquad (13)$$

The matrix M is defined by

$$M(\mathbf{K}, \lambda; \mathbf{K}', \lambda') = |\mathbf{K} \parallel \mathbf{K}'| \begin{pmatrix} \mathbf{e}_2 \cdot \mathbf{e}'_2 & -\mathbf{e}_2 \cdot \mathbf{e}'_1 \\ -\mathbf{e}_1 \cdot \mathbf{e}'_2 & \mathbf{e}_1 \cdot \mathbf{e}'_1 \end{pmatrix} \qquad (14)$$

In practice, the photonic band structure given by the frequencies $\omega(\mathbf{K}, \lambda)$ is computed over several high symmetry points in the Brillouin zone or on a grid in the Brillouin zone if the density of states is needed. Plane wave convergence is closely checked.

The first structure (19–21) considered by researchers was the fcc structure composed of low dielectric spheres in a high dielectric (ε) background. This simple structure with close packed spheres has the band structure shown in Fig. 8. There is no fundamental gap between the second and third bands—the bands are degenerate at the W point of the zone. There is a region of low densities of states between bands 2 and 3—the pseudogap, which may have interesting consequences. Another very interesting feature is a sizable complete gap between the 8 and 9 bands (8–9 gap), which exists over the entire zone (i.e., for all directions of propagation of the EM wave). The size of this gap is about 8% for a refractive index contrast of 3.1. The direct fcc structure (high dielectric spheres in a low contrast background), however, does not possess the dip in the photonic DOS.

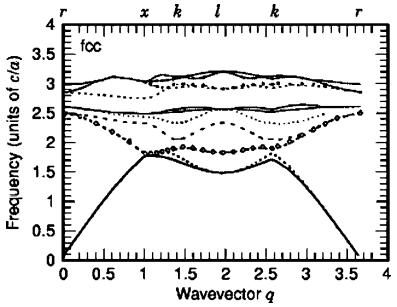

Figure 8. Photonic band structure for the fcc structure composed of air spheres in a high dielectric background (dielectric constant $e = 9.61$). The geometry is for close packed spheres (i.e., 74% filling ratio). The bands are shown along the 110 axis of the Brillouin zone.

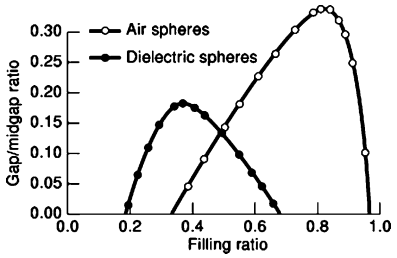

Figure 9. Size of the three-dimensional photonic band gap measured by the gap/midgap ratio for a diamond structure with spheres on the diamond sites and its conjugate structure. Band gaps are plotted as a function of the filling ratio. The dielectric contrast of 12.96 is used.

The diamond structure has been the subject of much investigation (<xref target="W4410-bib-0001 W4410-bib-0002 W4410-bib-0003 W4410-bib-0004 W4410-bib-0021 W4410-bib-0022" style="unformatted"/>) because it has a full three-dimensional photonic band gap between the fundamental bands (2–3 gap between the second and third bands). This gap exists for (1) high dielectric spheres on the sites of the diamond lattice (Fig. 9), (2) the diamond structure with low dielectric spheres on the diamond sites [Fig. 9; conjugate of (i)], and (3) the diamond structure connected by dielectric rods (Fig. 10).

The best performing gap (29%) is reached for the diamond structure with 89% air spheres (i.e., a multiply connected sparse structure). A similar large gap (30%) is also found for the diamond structure connected with dielectric rods with about 30% dielectric filling fraction. These gap magnitudes are for a refractive index contrast of 3.6, appropriate for GaAs.

A novel layer-by-layer structure was designed and fabricated at Iowa State University (24–30) (Fig. 3) with a full three-dimensional fundamental PBG (Fig. 11). The agreement between the calculated bands and the experimental measurements are excellent (Fig. 11) for both EM-wave

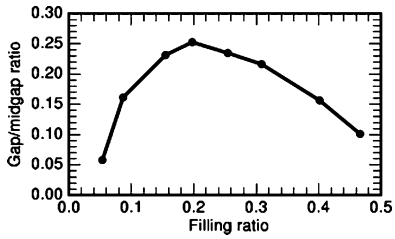

Figure 10. Size of the three-dimensional photonic band gap when the diamond structure is connected by dielectric rods (e = 12.96). Rectangular rods connect the sites in 111 planes, whereas cylindrical rods connect the rods along the 111 axis.

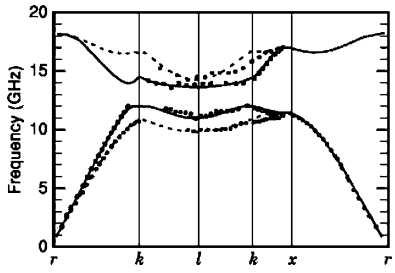

Figure 11. Calculated (lines) and measured photonic band structure for the layer-by-layer structure composed of stacked alumina cylinders (e = 9.61) with a full bandgap between 12 and 14 GHz. The circles represent measurements for the E-field polarization parallel to the rod axes, whereas the squares represent measurements performed with an E field perpendicular to the rod axes.

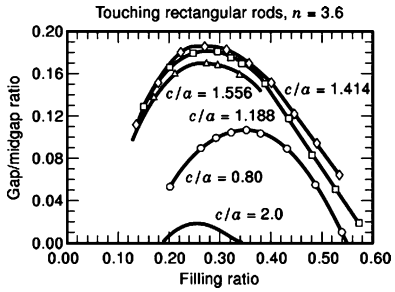

Figure 12. Size of the gap in the layer-by-layer structure as a function of filling ratio for different c/a ratios. c is the repeat distance, and a is the rod separation. A dielectric contrast of 12.96 has been used to facilitate comparison.

polarizations. This particularly robust structure has been fabricated at length scales providing gaps ranging from 13 to 500 GHz (24–30). As is typical for the diamond structure, the magnitude of the gap is maximized at about 25% (Fig. 12) for the contrast of n = 3.6. the densities of photon states for the experimentally fabricated structure with silicon micromachining (Fig. 13) provides a picture of both the fundamental gap and other frequency regions that display depleted or enhanced DOS.

The photonic band gap depends on (1) the local connectivity of the dielectric structure, (2) the contrast between the two media, and (3) the filling ratio. A minimum dielectric contrast ($\varepsilon > 4$) is usually needed to observe the band gaps. The photonic band structure method is a systematic way to search for the existence of band gaps in dielectric structures (3, 36).

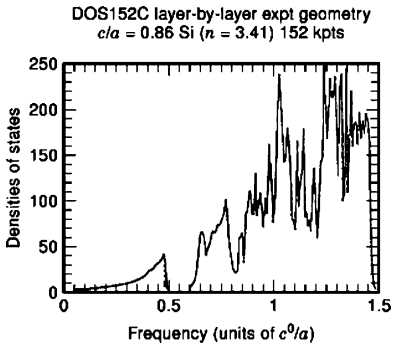

Figure 13. Photonic densities of states for the layer-by-layer structure using the experimentally fabricated geometry with a filling ratio of 0.26 and silicon (e = 11.67) as the dielectric material.

Transfer Matrix Method

Although the method described in the last section focuses on a particular wavevector, there are complementary methods that focus on a single frequency. In the transfer matrix method (*TMM*), first introduced by Pendry and MacKinnon (37), Eqs. (3) and (<xref target="W4410-mdis-0004" style="unformatted">4</xref>) are discretized, and the z components of the fields can be eliminated, so we derive the following equations:

$$\begin{aligned} E_x(i,j,k+1) = {} & E_x(i,j,k) + ic\omega\mu_0\mu(i,j,k)H_y(i,j,k) \\ & + \frac{ic}{a\omega\epsilon_0\epsilon(i,j,k)}\{a^{-1}[H_y(i-1,j,k) - H_y(i_1,j,k)] \\ & - b^{-1}[H_x(i,j-1,k) - H_x(i,j,k)]\} \\ & - \frac{ic}{a\omega\epsilon_0\epsilon(i+1,j,k)}\{a^{-1}[H_y(i,j,k) \\ & - H_y(i+1,j,k)] - b^{-1}[H_x(i+1,j-1,k) \\ & - H_x(i+1,j,k)]\} \end{aligned} \tag{15}$$

$$\begin{aligned} E_y(i,j,k+1) = {} & E_y(i,j,k) - ic\omega\mu_0\mu(i,j,k)H_x(i,j,k) \\ & + \frac{ic}{b\omega\epsilon_0\epsilon(i,j,k)}\{a^{-1}[H_y(i-1,j,k) - H_y(i,j,k)] \\ & - b^{-1}[H_x(i,j-1,k) - H_x(i,j,k)]\} \\ & - \frac{ic}{b\omega\epsilon_0\epsilon(i,j+1,k)}\{a^{-1}[H_y(i-1,j+1,k) \\ & - H_y(i,j+1,k)] - b^{-1}[H_x(i,j,k) \\ & - H_x(i,j+1,k)]\} \end{aligned} \tag{16}$$

$$\begin{aligned} H_x(i,j,k+1) = {} & H_x(i,j,k) - ic\omega\epsilon_0\epsilon(i,j,k+1)E_y(i,j,k+1) \\ & + \frac{ic}{a\omega\mu_0\mu(i-1,j,k+1)}\{a^{-1}[E_y(i,j,k+1) \\ & - E_y(i-1,j,k+1)] - b^{-1}[E_z(i-1,j+1,k+1) \\ & - E_z(i-1,j,k+1)]\} - \frac{ic}{a\omega\mu_0\mu(i,j,k+1)} \\ & \{a^{-1}[E_y(i+1,j,k+1) - E_y(i,j,k+1)] \\ & - b^{-1}[E_x(i,j+1,k+1) - E_x(i,j,k+1)]\} \end{aligned} \tag{17}$$

$$H_y(i,j,k+1) = H_y(i,j,k) + ic\omega\epsilon_0\epsilon(i,j,k+1)E_x(i,j,k+1) + \frac{ic}{a\omega\mu_0\mu(i,j-1,k+1)}\{a^{-1}[E_y(i+1,j-1,k+1) - E_y(i,j-1,k+1)] - b^{-1}[E_x(i,j,k+1) - E_x(i,j-1,k+1)]\} - \frac{ic}{a\omega\mu_0\mu(i,j,k+1)}\{a^{-1}[E_y(i+1,j,k+1) - E_y(i,j,k+1)] - b^{-1}[E_x(i,j+1,k+1) - E_x(i,j,k+1)]\} \quad (18)$$

$\varepsilon(i,j,k)$ and $\mu(i,j,k)$ are the dielectric constant and the magnetic permeability at the subcell (i,j,k). a, b, and c are the dimensions of each subcell along the x, y, and z directions. Equations (15)–(18) are connecting the fields at the $k+1$ plane with the fields at the k plane. Using TMM, the band structure of an infinite periodic system can be calculated, but the main advantage of this method is for the calculation of transmission and reflection properties of EM waves of various frequencies incident on a finite thickness slab of PBG material.

Such calculations are extremely useful in the interpretation of experimental measurements of transmission and reflection data. The TMM method can also be applied to calculate PBG structures containing absorptive and metallic materials. The TMM has previously been applied to defects in 2-D PBG structures (38), photonic crystals with complex and frequency dependent dielectric constants (39), metallic PBG materials (40,41), and angular filters (42). In all these examples, the agreement between theoretical calculations and experimental measurements was very good.

At this point, we return to the discussion of Fig. 7. There, we used a rectangular conventional unit cell consisting of 15×26 subcells. In order to create the triangular lattice, we placed cylinders at the corners and at the center of the rectangular unit cell. The system is finite along the z direction [see Fig. 2(a) having a thickness.of three unit cells. Along the x direction, we use a supercell consisting of three conventional unit cells, and we assume periodic boundary conditions at the edges of the supercell. So, there are infinitely many defects along the x direction with separation of $3a$. This is the reason for the small change in the frequency as we change the angle. Calculations with larger supercells (consisting of five conventional unit cells) show negligible angular dependence.

Finite Difference Time Domain Method

Even though the preceding transfer matrix method is employed for steady state solutions, the finite difference time domain (*FDTD*) method is used for general time-dependent solutions including transient behavior. In this method, the Maxwell curl equations are numerically solved:

$$\nabla \times \mathbf{E} = -(1/c)\frac{\partial \mathbf{H}}{\partial t} \quad (19)$$

$$\nabla \times \mathbf{H} = (1/c)\epsilon(\mathbf{r})\frac{\partial \mathbf{E}}{\partial t} \quad (20)$$

The derivatives in the Maxwell's equations are approximated with finite differences and the electromagnetic fields components are located on a Yee cell (43). In the Yee cell, the E-field components at time $n\Delta t$ are located on the sides of a cube. The magnetic field H components at times $(n + 1/2)\Delta t$ are located at the face-centered points of the Yee cell. This results in both spatial and temporal offsets of the two fields when the Maxwell curl equations are solved on each face of the cube. The system is described by a spatial grid. The time step is chosen such that an EM wave will propagate less than a grid spacing during the time step.

$$E_x^{n+1}(i,j,k) = E_x^n(i,j,k) + \frac{\Delta t}{\epsilon(i,j,k)}\left[\frac{H_z^{n+1/2}(i,j+1/2,k) - H_z^{n+1/2}(i,j-1/2,k)}{\Delta y} - \frac{H_y^{n+1/2}(i,j,k+1/2) - H_y^{n+1/2}(i,j,k-1/2)}{\Delta z}\right] \quad (21)$$

$$E_y^{n+1}(i,j,k) = E_y^n(i,j,k) + \frac{\Delta t}{\epsilon(i,j,k)}\left[\frac{H_x^{n+1/2}(i,j,k+1/2) - H_x^{n+1/2}(i,j,k-1/2)}{\Delta z} - \frac{H_z^{n+1/2}(i+1/2,j,k) - H_z^{n+1/2}(i-1/2,j,k)}{\Delta x}\right] \quad (22)$$

$$E_z^{n+1}(i,j,k) = E_z^n(i,j,k) + \frac{\Delta t}{\epsilon(i,j,k)}\left[\frac{H_y^{n+1/2}(i+1/2,j,k) - H_y^{n+1/2}(i-1/2,j,k)}{\Delta x} - \frac{H_x^{n+1/2}(i,j+1/2,k) - H_x^{n+1/2}(i,j-1/2,k)}{\Delta y}\right] \quad (23)$$

$$H_x^{n+1/2}(i,j,k) = H_x^{n-1/2}(i,j,k) + \frac{\Delta t}{\mu(i,j,k)}\left[\frac{E_y^n(i,j,k+1/2) - E_y^n(i,j,k-1/2)}{\Delta z} - \frac{E_z^n(i,j+1/2,k) - E_z^n(i,j-1/2,k)}{\Delta y}\right] \quad (24)$$

$$H_y^{n+1/2}(i,j,k) = H_y^{n-1/2}(i,j,k) + \frac{\Delta t}{\mu(i,j,k)}\left[\frac{E_z^n(i+1/2,j,k) - E_z^n(i-1/2,j,k)}{\Delta x} - \frac{E_x^n(i,j,k+1/2) - E_x^n(i,j,k-1/2)}{\Delta z}\right] \quad (25)$$

$$H_z^{n+1/2}(i,j,k) = H_z^{n-1/2}(i,j,k) + \frac{\Delta t}{\mu(i,j,k)}\left[\frac{E_x^n(i,j+1/2,k) - E_x^n(i,j-1/2,k)}{\Delta y} - \frac{E_y^n(i+1/2,j,k) - E_y^n(i-1/2,j,k)}{\Delta x}\right] \quad (26)$$

$E^{n}{}_{x}(i, j, k)$ is the x component of the electric field at the n time step in the (i, j, k) subcell.

Finite size systems can be easily modeled. This widely used technique (44,45) can be used to find either the steady state or transient response of arbitrary systems containing dielectric or metallic components, as well as materials with nonlinear dielectric properties. In the perfect metallic code, the E field vanishes inside the metal. The FDTD can be used with a Gaussian pulse source. The fields are numerically integrated to obtain the fields at long times (>1000 time steps). The Fourier transform of the scattered and incident fields generates the frequency-dependent response of the system. Alternatively, the system may be subject to a source field with a single frequency ω, and one can determine the steady state response of the system at that frequency. Such steady state calculations may then be repeated at desired frequencies.

At the edges of the FDTD cell, outer radiation boundary conditions are frequently employed. Here the incident wave at the boundary is absorbed. Methods to transform the near fields to radiating far fields are then employed. This is particularly necessary for antenna problems where far-field radiation patterns are desired. The FDTD method is a very powerful design tool in simulating the electromagnetic response of systems, covering a broad range of frequencies.

We have used this method to calculate the radiation patterns of dipole antennas placed on PBG crystals (Fig. 14). The dipole antenna is driven by either a voltage pulse or a steady-state sinusoidal excitation, and the radiated far fields are determined. The symmetry of our PBG crystal has been used to develop a computational cell that is one fourth the size of the actual system (46). The calculations are in very good agreement with measurements (46). It is also possible to calculate the currents flowing in the antenna and to calculate the gain of the system. We have driven a finite length dipole oscillator on the surface of the PBG crystal at a frequency of 13 GHz near the center of the band gap. The dipole is at the intersection of the first and second layers, and the radiation patterns are calculated and measured at different heights z above the surface (Fig. 14). The agreement in both the E and H planes with measurements is very good.

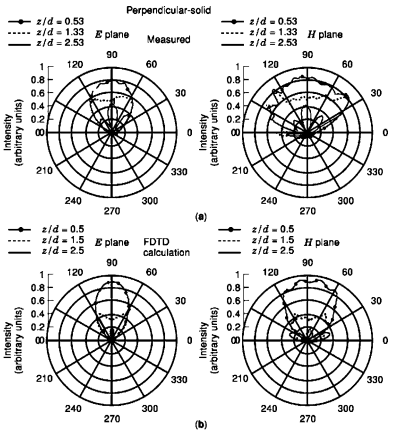

Figure 14. Measured (a) and FDTD calculations (b) of the antenna radiation in the E and H planes for a dipole antenna driven at 13 GHz at the center of the PBG. The three curves are for different heights z of the antenna above the surface, expressed as a ratio of z/d where d is the diameter of the dielectric rod. The antenna is at the intersection of the first and second layers, perpendicular to the first layer.

Scattering matrix method- Fourier space transfer matrix method

While early calculations were performed with this real space transfer matrix method, it has been found to be more convenient and accurate to use the transfer matrix method in a plane wave basis where Maxwell's equations are solved in Fourier space [48]. The structure is divided into slices (along the z axis). In each slice the dielectric function ε(r) is a periodic function of the planar coordinates (x,y). Hence the dielectric function and its inverse are expressed as a Fourier expansion with coefficients ε(G) or ε^{-1}(G), where **G** are the reciprocal lattice vectors of the 2-dimensional lattice. The electric and magnetic fields also have Fourier coefficients **E**(**G**) and **H**(**G**) defined through

$$E_k(r) = \sum_G E_G(z) e^{i(k+G)x_{||}}$$

where k is a Bloch wave-vector.

From the six Maxwell equations for each Cartesian component of the **E** and **H** fields, the z-component of the **E** and **H** field is eliminated leading to four equations for the z-derivatives of the x,y components of the **E** and **H** fields. We adopt a recently developed formulation [47,48] where the transfer matrix is computed in Fourier space. In each layer a transfer matrix M_1 relates the z derivative of the electric field to the fourier components of the **H** field and a similar equation for the z-derivative of the **H** field with a transfer matrix M_2. This results (28) in a single eigenvalue equation for the **E** field in each layer involving the transfer matrix M. The transfer matrix M is diagonalized to obtain the eigenmodes within each layer. Both polarizations are included. The transfer matrix M in each layer is calculated that relates the z-dependence of the **E**, **H** fields in each layer.

$$\frac{\partial}{\partial z} E = M_1 H; \frac{\partial}{\partial z} H = M_2 H$$
$$\frac{\partial^2}{\partial z^2} E = M_1 M_2 E = ME$$

We have employed a compact notation where **E** and **H** in (28) represents the matrix of Fourier coefficients **E**(G), **H**(G) and M, M_1 and M_2 are corresponding square matrices. The propagation wave vectors (k_z) from this eigenmode problem determine whether the mode is propagating or decaying. The boundary conditions are that the parallel components of **E** and **H** are continuous at each interface and this leads to the individual scattering matrices s_i of each layer.

A standard recursion algorithm [48,50] combines the scattering matrices of each layer into the scattering matrix S for the entire structure. Using the total S-matrix, we

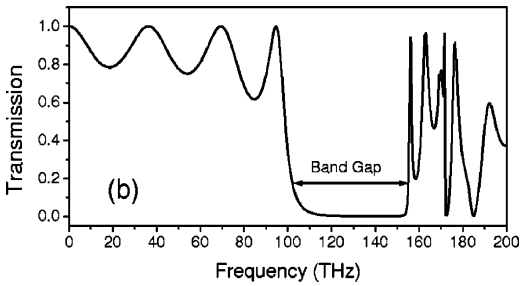

Figure 15. Simulated transmission spectrum for a 8-layer layer-by-layer photonic crystal slab along the 001 direction. The polarization of the incident wave is such that the electric field is parallel to the rods in the first layer. The dielectric constant is $|*\text{epsilon}*| = 12$, the filling ratio is f=0.3, and the lattice spacing is $1|*\text{mu}*|$.

simulate the reflection and transmission of the structure when fields are incident from the left. The advantage of this Fourier space approach is that any number of layers of differing width can be easily simulated since a real-space grid is not necessary. Since the solutions of Maxwell's equations are independent for each frequency, the computational algorithm has been parallelized on massively parallel systems, where the transmission/reflection for each frequency is solved on a separate processor.

This method relies on the convergence of the plane wave expansion of the fields, which depends on the type of structure being simulated. For structures where each layer has 2-dimensional periodicity both polarizations are solved for leading to a matrix size of $N = 2N_G$ where N_G is the number of plane waves. For dielectric systems the number of plane waves (N_G) can be less than $\sim$150 for reasonable convergence. For metallic systems, considerable larger number of plane waves (>500) are necessary [49].

For the layer-by-layer structure, each layer has 1-dimensional periodicity. This leads to the transfer matrix solution decomposing into separate solutions for the TE and TM modes, and a matrix of size N_G is to be solved. We illustrate this method by the calculated transmission for a layer-by-layer photonic crystal (Fig. 15) with a fourier expansion of 13×13 plane waves. By enforcing periodic boundary conditions along the crystal axes the photonic band structure can also be computed with this method [47].

EXPERIMENTAL TECHNIQUES FOR FABRICATION OF PHOTONIC BAND GAPS

There have been intensive efforts to build and test photonic band gap structures, dating back to the original efforts of Yablonovitch shortly after his first proposal for PBG crystals (51). Fabrication can be either easy or extremely difficult, depending on the desired wavelength of the band gap and the level of dimensionality. Because the wavelength of the band gap scales directly with the lattice constant of the photonic crystal (3, 52), lower-frequency structures that require larger dimensions will be easier to fabricate. At microwave frequencies, where the wavelength is on the order of 1 cm, the photonic crystals are decidedly macroscopic, and simple machining techniques or rapid prototyping methods can be employed in building the crystals. At the other extreme, optical wavelength PBGs require crystal lattice constants less than 1 μm. Building PBGs in the optical regime requires methods that push current state-of-the-art micro- or nanofabrication techniques. In a similar manner, the dimensionality of the PBG has a big impact on the ease or difficulty of fabrication. Because one-dimensional PBGs require periodic variation of the dielectric constant in only one direction, they are relatively easy to build at all length scales. One-dimensional PBG mirrors (more commonly known as distributed Bragg reflectors (DBR)) have been used in optical and near-infrared photonic devices for many years. Two common examples of devices using 1-D PBGs are distributed feedback lasers and vertical-cavity surface-emitting lasers. Two-dimensional PBGs require somewhat more fabrication, but relatively mainstream fabrication techniques can be employed to achieve such structures. There are several examples of 2-D PBGs operating at mid- and near-IR wavelengths. Clearly, the most challenging PBG structures are fully 3-D structures with band gaps in the IR or optical regions of the spectrum. The fabrication of 3-D PBGs is complicated by a need for large dielectric contrast between the materials that make up the PBG crystal and the relatively low filling fractions that are required. The large dielectric contrast means that the materials must be dissimilar, and often the low-dielectric material is air with the other material being a semiconductor or a high-dielectric ceramic. The low filling fraction means that the PBG crystal with air as one dielectric will be relatively empty and the high dielectric material must be formed into a thin network or skeleton. When these difficulties are combined with a need for micron or submicron dimensions to reach into the optical region, the fabrication becomes very difficult, indeed. This area of PBG research has been one of the most active, and perhaps most frustrating, in recent years.

The various methods to synthesize photonic crystals can be divided into two main groups: (1) methods that use (or extend) conventional semiconductor microfabrication techniques and (2) non-semiconductor techniques. The following list of processing methods is meant only to give some flavor for current avenues toward achieving PBGs. We focus on 3-D photonic crystals and 1-D and 2-D PBGs are not be included.

Semiconductor-Based Methods

Advanced semiconductor processing. A novel method to fabricate 3-D photonic crystals using state-of-the-art semiconductor processing techniques was pioneered by the Sandia group of S. Lin, J. Fleming and co-workers (53), and has been most successful in fabricating the layer-by-layer structure, first at a pitch of 4.2 μ (53) -corresponding to a gap wavelength of 10 μ, and then (54) at a pitch of 0.6 μ (with a gap wavelength of 1.5 μ). The 1.5 μ wavelength is critical for fiber-optic telecommunications applications. In this technique, the vertical topology of the 3D lattice structure is built by the repetitive deposition and etching of multiple dielectric films and a systematic multi-layer stacking process was developed. Within each layer, SiO2

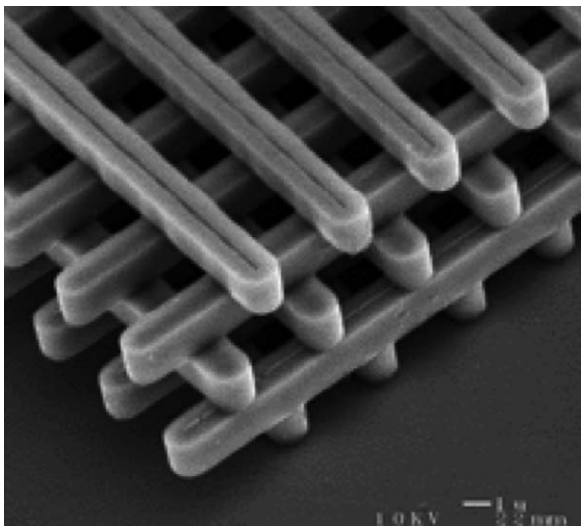

Figure 16. Transmission electron micrograph of the 3-D layer-by-layer photonic crystal with a bar spacing of a = 4.2| ∗ mu ∗ |, fabricated by advanced silicon processing methods (Ref 53).

was first deposited, patterned in the required 1-d pattern, and etched to the desired depth. The resulting trenches were then filled with polycrystalline silicon. Following this, the surface of the wafer was planarized using chemical mechanical polishing, and the entire process was then repeated. The planarization step is critical for producing a flat surface for the deposition of the next layer and a repetition of the processing scheme. After the multi-layer process was completed, the wafer was immersed in a HF/water solution for the removal of the SiO_2. Samples with 5-layers of the layer-by-layer structure with a complete band gap were fabricated. Figure 16 shows a scanning electron micrograph (SEM) top view of a completed four-layer structure. The strongest attenuation occurs at 10-11 μ, with an attenuation strength of 12 dB per unit cell. The dependences of the band edges with angle of incidence confirm that the structure has a complete photonic gap.

A variation of this planarization method (54) using filet processing was able to double the periodicity possible with a deposited SiO_2 pattern, and was used to create a photonic crystal with a minimum feature size of 0.18 μ, and a band gap around 1.5 μ.

Closely following these developments the group of Noda et al (55) fabricated a III-V photonic band gap crystal with a midgap wavelength of 1.4 μ. In this method, III-V semiconductor stripes (of GaAs or InP) were fabricated and then stacked with the wafer-fusion method. Precise alignment was achieved by laser-beam assisted aligning and a pitch of 0.7 μ was achieved. An attenutation of 40 dB was achieved with a 4-layer structure. Wafer fusion was best achieved at temperatures around 500 C. Because the crystal is constructed with III-V semiconductors, these are very suitable for optoelectronic devices. A sharp waveguide bend was also fabricated (55) by removing two rod segments.

These pioneering achievements opened the field for further advanced semiconductor processing of the layer-by-layer structure at optical and near infrared length scales. Subramania and Lin (56), fabricated a 5-layer by layer structure with electron beam lithography and spin on glass planarization (56). A rod spacing of 0.66 μ was achieved with a rod width of 0.22 μ for a five-layer structure. Rod spacings of 0.5 μ and 0.55 μ were also achieved. A reflectance peak spanning the near-IR range from 1.2-1.5 μ was observed for this family of structures, indicative of the band gap.

Similar methods have also been employed (57) to fabricate metallic photonic crystals by deposition of tungsten into the patterned SiO_2 layer and repeating the procedure. The SiO_2 was also etched off to produce a 5-layer metallic layer-by-layer photonic crystal with a pitch of 4.2 μ. The optical properties of tungsten photonic crystals fabricated with this technique have been further measured by Seager et al. (58).

Vertical Reactive-Ion Etching. Vertical reactive-ion etching to form 2-D PBGs (59–62) is perhaps most straightforward technique because it derives directly from current microfabrication methods. The 2-D PBG is formed in a GaAs/(Al, Ga)As dielectric waveguide grown on a GaAs substrate using epitaxial growth techniques. The 2-D PBG consists of a square or triangular array of holes that are etched through the dielectric waveguide. Either electron beam lithography (59–61) or holographic patterning was used to define the 2-D pattern on the surface of the wafer. Then dry etching techniques are used to etch the holes down 1 μm or more. Lattice constants for the works cited here were in the range of 190–480 nm. The measured optical properties of the waveguide-PBG system in 59–61 showed clear transmission stop bands or strong reflection bands in the IR spectrum. O'Brien et al. (60) used the PBG as one mirror of a *QW* laser.

Superlattice Disordering and Selective Oxidation. Use of superlattice disordering and selective oxidation to form 2-D PBGs (63) achieves structures that are similar to those described in the previous section. The starting material is an epitaxially grown GaAs/AlAs multilayer structure. Silicon nitride is deposited on the top surface, and holes are etched into the silicon to expose the top surface of the wafer. In the reported work, the holes were arrayed in a triangular lattice pattern, with a hole diameter of 2 μm and a lattice constant of 8 μm. After the holes were etched, zinc was diffused into the semiconductor crystal through the openings. The diffusing zinc disorders the multilayer structure, converting it to a homogeneous (Al, Ga)As alloy. After the diffusion, the structure is exposed to an oxidizing ambient, and the disordered regions are selectively converted to aluminum oxide. Thus, the resulting structure is a GaAs/AlAs multilayer with a regular array of oxide posts inserted. The authors used this structure to build a photo-pumped semiconductor laser.

Deep Anodic Etching of Silicon Wafers. Deep anodic etching of silicon wafers to form 2-D PBGs (64) is similar in concept to vertical reactive-ion etching, differing in starting materials and scale. The material is silicon. A 2-D array of small starter etch pits is formed on the surface using standard patterning and etching techniques. Typical dimensions and lattice constants are on the order of 2–10

μm. Then, a photo-induced anodic etching procedure is employed.

Macropores can be formed in the 110 direction in a n-doped Si wafer if it is anodized in an HF solution and illuminated from the backside. The illumination creates electron-hole pairs and the electrons migrate to the growing etch pits. With careful control of the anodic etching, the pattern of holes can be extended through the entire thickness of the wafer—more than 400 μm—leading to a much thicker 2-D structure than can be achieved using the GaAs techniques described previously. The transmission spectrum of the fabricated structures showed distinct stop bands in the mid-IR region. This technique has been repeated for submicron lattice constants (65). It should be noted that without the use of a patterned silicon wafer, a random array of etch pits is produced in a porous silicon structure (66) which also has very interesting 1-D photonic crystal properties.

True three-dimensional structures have not yet been demonstrated using semiconductor techniques, although there are several proposed routes toward optical PBGs.

Three-Cylinder PBG Using Directional Ion Beam Etching. The basic approach (67) uses a scaled-down version of Yablonovitch's three-cylinder PBG proposed and demonstrated at microwave frequencies (23). The starting material is again GaAs. A masking layer of SiN and AlO is formed on the surface of a GaAs wafer, and then a triangular array of holes is etched through the masking layer to expose the underlying GaAs. Then a series of three angled ion beam etching steps is performed. Each etch step forms a deep array of etch pits angled at 35° off normal. After the first etch step, the GaAs substrate is rotated by 120°, a second is etched, the substrate is rotated again, and the third set of holes is drilled. The result is a set of intersecting air cylinders that form a diamond-like lattice structure in the GaAs crystal. Using electron-beam lithography, submicron dimensions are possible. Structurally, the photonic crystal clearly exhibits two or three unit cells. However, optical measurement has not shown the expected photonic band gap. The most likely cause of the lack of band gap is non-uniformity in the etching profile. Further research continues on this avenue of PBG fabrication.

Nonsemiconductor Methods

Laser Rapid Prototyping. (31) Laser chemical vapor deposition has been used to fabricate a layer-by-layer structure similar to the one described in Fig. 3. The photonic crystal consisted of aluminum oxide rods, and the measured photonic band gap was centered at 2 THz. The index contrast may be lower than expected due to the porosity of the material. Further experiments on this promising direction are needed.

Deep X-Ray Lithography. (68) *PMMA* resist layers with thickness of 500 μm were irradiated in order to form a three-cylinder structure. Because the dielectric constant of the PMMA is not enough for the formation of a photonic band gap, a molding step must be applied. The holes in the resist structure were filled with solution of polyvinylsilazane in tetrahydrofuran. After the evaporation of the solvent, the samples were pyrolyzed at 1100 °C under N_2 atmosphere. The resist decomposes into CO_2, CH_4, CO, and H_2O, whereas polyvinylsilazane is transformed into SiCN ceramic. A lattice of ceramic rods corresponding to the holes in the resist structure remained. Calculation using the transfer matrix method showed that the dielectric constant of the ceramic should be around 3.5 in order to fit the measured band gap centered at 2.5 THz. This is an indication that the ceramic was quite porous. Further work is needed for the fabrication of photonic crystals with more compact ceramic material, which hopefully will give higher dielectric constants. More recently, two- and three-dimensional nanostructures of TiO_2 were fabricated (69) using x-ray lithography and liquid-phase deposition. Using deep X-ray lithography a PMMA template was formed with an array of nano-order holes having a high aspect ratio. This template was filled with dense TiO2 by liquid-phase deposition. A novel 3-D photonic crystal structure of slated pores that could be achieved with X-ray lithography, was theoretically predicted (70) to have a band gap of 28%.

Holographic Methods. Holography is a complementary approach to layer-by-layer methods in that the entire 3-D photonic crystal can be fabricated at the same time and has been an extremely active area of ongoing research (71–76). In holography a multiple beam of lasers is incident on a thick photoresist layer, providing a three-dimensional interference pattern. The photoresist is then developed. Negative photoresists exhibit a certain exposure dose threshold, above which the resist is not soluble in the developing process. Thus the spatial intensity of the dose gets transferred into the distribution of matter, resulting in a porous polymeric structure, the shape of which is tailored by the laser interference pattern. For positive photoresists, the underexposed regions remain after development.

The photoresists have low refractive index contrast making them unsuitable for full photonic band gaps. Thus infiltration of higher index material (such as silicon) is necessary to improve the refractive index contrast, followed by removal of the resist altogether.

The mathematical process of the interference pattern has been investigated in detail (73, 75). Generally four laser beams are necessary for formation of three-dimensional photonic crystals with complete band gaps. Structures close to the three-hole structure having rhombohedral symmetry have been predicted from 4-beam holography. Such structures can have complete band gaps of 5% or larger for suitable filling ratios (38%) and structural parameters (75). Five holographic beams propagating from the same half-space has been predicted (75) to yield band gaps of 25% when the exposed photoresist is replicated with silicon. Genetic algorithms have also been utilized (76) to predict holographic structures with band gaps of 28%, similar to a rod-connected diamond structure.

Self- Assembled Photonic Crystals. Theoretical studies (77, 78) have identified the "inverse" face-centered cubic (fcc) structure as one of the best suited for photonic band gaps. This consists of a periodic array of close-packed low dielectric spheres with refractive index n_1 in a high dielectric background with refractive index n_2, generating

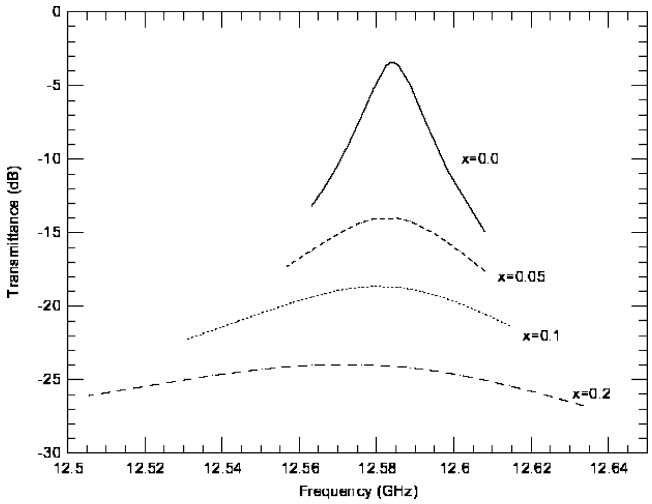

Figure 17. Densities of photon states for the fcc structure of air spheres in a dielectric medium of refractive index 3.6. The filling ratio of air is 74%.

the refractive index contrast $n=n_2/n_1$. The spheres may be air (n_1=1) enclosed by the interconnected higher dielectric background. Calculations have found the inverse fcc structure to have both a low-frequency pseudogap between bands 2 and 3 where the density of photon states reaches zero, and a high frequency three-dimensional band gap between higher bands 8 and 9 (Fig. 17; Fig. 8) . The gap is $\sim$5% in magnitude for a refractive index contrast of 3.5. Generally a higher refractive index contrast ($>$2.4) is necessary to observe the full band gap. The inverse structure has much more desirable photonic gaps than the direct structure of close-packed dielectric spheres. Other stacking sequences such as hexagonal close-packed and double-hcp also yield high band gaps (79). .

We have also achieved this inverse opal structure by a somewhat different ceramic technique where the ordering and filling process was performed simultaneously (88, 89). The starting point was a slurry of nanocrystalline titania which was mixed with a suspension of polystyrene spheres (88, 89). On drying of this slurry on a slide, ordering of the spheres was observed in a region of the slide evidenced by a band of color. The spheres were ordered and the interstitial regions were filled by the titania nanoparticles. The spheres were then removed by calcination above 200 C, leaving a macroporous solid where close-packed spherical air cavities are enclosed by a high dielectric matrix. It was necessary to sinter the titania near 550 C to densify it and improve the refractive index contrast (88, 89).

The inverse opal structure was preceded by ordered structures of monodisperse spheres which did not have appreciable photonic band gaps but did exhibit stop bands (90–93) from the band gaps along the stacking direction.

Robotic Micromanipulation. Robotic micromanipulation is a very specialized technique for fabricating precise three-dimensional photonic crystals of small sizes.

Micromanipulation of two different size spheres has been employed to buld up a diamond lattice (94). This was then back-filled with silicon to generate an inverse opal diamond-like lattice in silicon (94). Micromanipulation of bars of InP were performed to build up the layer-by-layer photonic crystal with a pitch of 1.4 μ (95). A band gap at wavelengths between 3-4 μ was observed in a 4-layer sample that measured 15 μ $\times$ 15 μ in size.

Soft Lithographic Methods. Soft lithography using microtransfer transfer molds has evolved into a very popular technique for generating economical large area photonic crystals, down to infrared and optical length scales. The basic principle is based on transferring a whole layer of polymer pattern using an elastomer mold onto a substrate or multilayer polymer template (96–98).

The starting point is to create a master stamp which is typically a silicon wafer on which a patterned photo resist is created by standard photolithographic methods. Typically photo resist is spun on to a silicon wafer and exposed to a patterned mask and then developed and baked. For the layer-by-layer structure this pattern consists of a one-dimensional layer of rods. The next step is to create an elastomeric mold from the master stamp. After the PDMS is cured, it is removed gently from the master stamp resulting in a relief structure on the elastomeric mold. The third step is to fill the troughs of the PDMS with epoxy. Care is taken to not overfill the epoxy; otherwise excess epoxy can spill over into the underlying layers. One way to fill with epoxy is to put a tiny drop of epoxy on the PDMS mold and drag the drop with a wire across the surface. The epoxy can be oven cured. In the final step the epoxy filled PDMS is placed in contact with a glass or silicon substrate. After the epoxy has hardened the PDMS is peeled off leaving a set of parallel epoxy rods on the substrate and one layer of the polymer template is thus created.

The second and subsequent layers are fabricated in the same manner, except the epoxy filled elastomeric mold is applied to a one-layer or multi-layer structure on the substrate. By repeating this synthesis a multi-layer structure can be fabricated. Alignment of third and subsequent layers is a major concern in this method. It has proved to be very fruitful to align using the technique of Moire fringes and identify well-aligned regions in the sample. Layer-by-layer photonic crystals with pitch of 2.5 and 1 μ have been fabricated with this method, which can be extended into the optical length scale. Dielectric and metallic structures have been fabricated with this technique.

3-D PHOTONIC CRYSTALS WITH DIELECTRICS

In this section, we study some of the recent achievements in the field, and we point out some of the difficulties that may rise in the future especially for photonic crystals operating at the optical frequencies. We start with the defect cases.

We study 3-D layer-by-layer photonic crystals (24–30). The structure is made of layers of cylindrical alumina rods with a stacking sequence that repeats itself every four layers with repeat distance, c = 1.272 cm. Within each layer, the rods are arranged with their axes parallel and separated by a distance a = 1.123 cm. The orientations of the axes are rotated by 90° between adjacent layers. To obtain

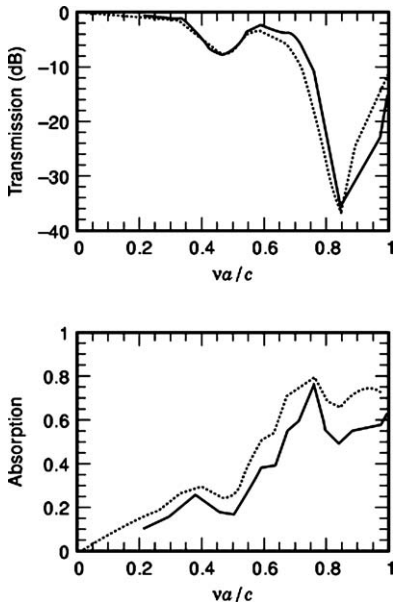

Figure 18. The transmission of EM waves propagating through a 3-D layer-by-layer PBG consisting of 16 layers of rods. The dotted lines correspond to the periodic case, whereas the solid lines correspond to the defect case in which every other rod from the eighth layer has been removed. Panels (a) and (b) correspond to the polarization with the electric field parallel and perpendicular to the first layer of rods.

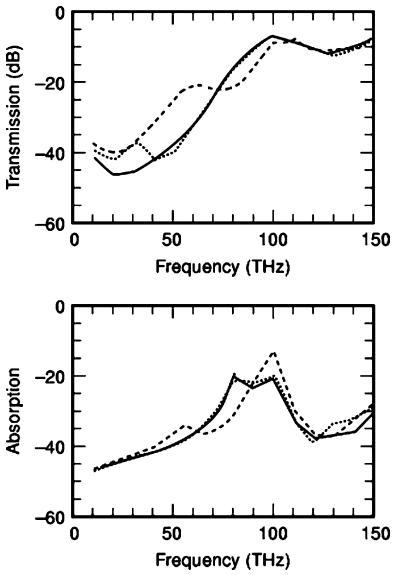

Figure 19. The transmission of EM waves propagating in a system similar to the one described in Fig. 18. The dielectric constant of the rods is | ∗ epsilion ∗ | = 9.61 + ix. E field is parallel to the axis of the removed cylinders. Curves are for different values of the absorption x.

the periodicity of four layers in the direction of stacking, the rods of the second neighbor layers are shifted by a distance of $a/2$ in the direction perpendicular to the rods axes (24–30). In order to simulate this structure with the real space TMM, we divide the unit cell into $7 \times 7 \times 8$ subcells assuming that the z axis is along the stacking direction.

Figure 18 shows the transmission of EM waves incident on a layer-by-layer photonic crystal with four unit cell thickness (16 layers of rods). The k vector of the incident wave is along the stacking direction (z axis). For the periodic case (dotted lines in Fig. 18), there is a gap between 11 and 15.7 GHz for both polarizations. We introduce a defect in this structure by removing every other rod in the eighth layer. A defect peak appears at 12.58 GHz. The width of the peak (0.016 GHz) is almost the same for both polarizations, and the transmission at the top of the peak (-3.4 and -29.7 dB for each polarization) is higher for the polarization where the incident electric field is parallel to the axis of the removed rods. In general, the transmission for the parallel polarized waves is more affected by the defect than the perpendicular polarized waves. The Q factor and the defect frequency are in very good agreement with measurements in the same configuration (30). However, the measured transmission at the top of the peak is about 10 dB smaller than that calculated, most probably because of some small absorption of the alumina rods (30). By increasing the thickness to eight unit cells (32 layers of rods), the width of the peak becomes 10^{-6} GHz, which corresponds to Q greater than 10^6, whereas the defect frequency and the transmission at the top of the peak remain almost the same (12.61 GHz and -3.8 dB, respectively).

In the optical wavelength region, the dielectric constant of most materials has an appreciable imaginary part. In order to study the effect of the absorption on the peak transmission resulting from defects, we calculated the transmission of a layer-by-layer structure with a defect (Fig. 19). The structure is similar to the one described in Fig. 18, in which we removed every second rod from the eighth layer (the system contains 16 layers of rods). We assume that the dielectric constant is given by

$= 9.61 + ix$. Increasing the imaginary part of the dielectric constant, the Q, as well as the transmission at the peak, decreases. In particular, $Q = 800$, 262, 163, and 90 for $x = 0$, 0.05, 0.1, and 0.2, respectively, whereas the transmission at the peak is -3.4, -14.0, -18.7, and -24.0 dB (Fig. 16). The introduction of the absorption makes the peak wider and the transmission on the peak smaller.

Even in periodic structures, the effect of the absorption could significantly change the transmission. Figure 20 show the transmission of a periodic layer-by-layer structure similar to the one described in Fig. 18 with three unit cells thickness. The real part of the dielectric constant is 9.61. By increasing the imaginary part, the transmission decreases at all the frequencies. Especially at the upper edge of the gap, the transmission has dropped by almost 10 dB compared to the case with zero imaginary part. In the non-absorbing cases, it is commonly accepted that the photonic crystal must be as thick as possible because the transmission inside the gap decreases as the thickness of the crystal increases. However, in photonic crystals constructed of materials with significant absorption, the transmission is thickness-dependent at all frequencies. So, it is possible that we will not be able to measure the transmission at the upper edge of the gap, which is more affected by the absorption, if it is less than the noise level of our measurements.

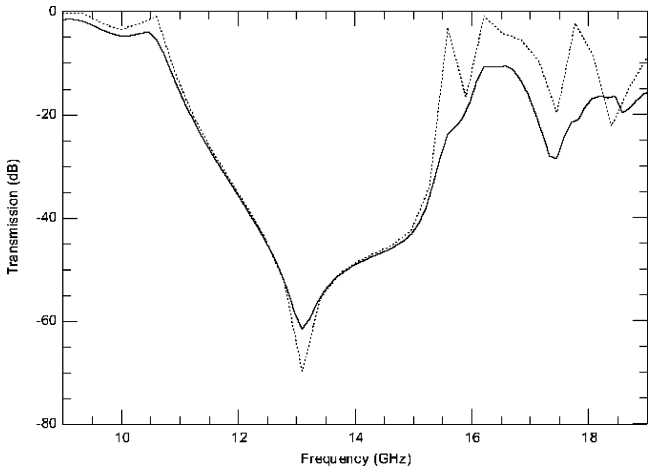

Figure 20. The transmission of EM waves propagating in a layer-by-layer system similar to the one in Fig. 4 with three unit cells thicknesses. The dielectric constant of the rods is | ∗ epsilion ∗ | = 9.61 + ix, where x is 0 and 0.2 (dotted and solid lines, respectively).

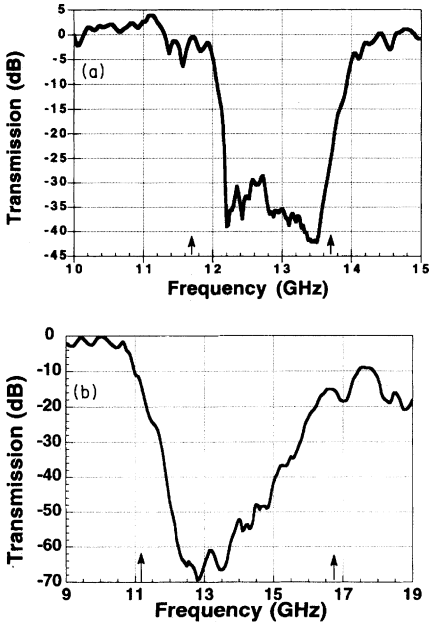

Figure 21. Measured transmission of electromagnetic waves incident a) along the x-axis (in the plane of the rods) and b) along the stacking direction (z-axis) of the layer-by-layer structure made with alumina rods. A rod spacing of 1.1 cm was used.

We show for comparison the measured transmission (Fig. 21) of EM waves incident from the top (z-axis) and from the side (x-axis) of the layer-by-layer photonic crystal composed of dielectric rods, with a spacing of 1.1 cm (25). The wider band gap along the stacking direction as predicted from the theoretical calculations is clearly evident.

Very sharp defect states with high Q can be created with defects within the 3-D photonic crystal. Various point defects in the InP layer-by-layer photonic crystal have been synthesized by S. Noda et al (99) at infrared frequencies, by either removing potions of rods or adding material. Cavity modes were observed at these point defect sites. It should be notedfor comparison that the highest Q defect with a Q exceeding 105 has been achieved by S. Noda and collaborators (<xref target="W4410-bib-0099 W4410-bib-0100" style="unformatted"/>) in a two-dimensional heterophotonic crystal. This 2-D photonic crystal has a defect region of slightly different lattice constant (100, 101), sandwiched between the regular lattice constant material.

The field of 3-D photonic crystals has been very rich with examples of alternative photonic crystal structures with complete photonic band gaps. The simple-cubic lattice has a fundamental photonic gap between the lowest bands 2 and 3 with a magnitude of ∼6% for a refractive index contrast of 3.6. When spheres are introduced on the lattice sites and connect to each other with narrow dielectric rods, a higher band gap between bands 5 and 6 opens up and reaches a maximum value of 12% (102) for a refractive index contrast of 3.6. The simple cubic lattice of rods was also fabricated at infrared frequencies, showing the expected band gap (103).

An alternative 3-D photonic crystal was designed by Johnson and Joannopoulos (104). This 3-D periodic dielectric structure with a large complete photonic band gap (PBG) consists of a structure with a sequence of planar layers, identical except for a horizontal offset, and repeating every three layers to form an fcc lattice. The layers can be thought of as an alternating stack of the two basic two-dimensional (2D) PBG slab geometries: rods in air and air cylinders in dielectric. These high-symmetry planar cross-sections may simplify the integration of optical devices and components by allowing modification of only a single layer, using simple defects of the same form as in the corresponding 2D systems. Gaps of over 21% are obtained for Si/air substrates. Reasonable gaps, over 8%, were achieved even for the moderate index ratio of 2.45 (Si/SiO_2). A different 3-D photonic crystal layered photonic crystal structure was also designed (105). This has a connectivity that is different from diamond and possesses square symmetry within each layer. This structure has a complete photonic band gap of 18% of the midgap frequency with a dielectric contrast of 12:1. A waveguide in this crystal was created by removing a row of rods from a single layer.

A planar diamond structure with triangular lattice meshes, supported by vertical rods was also developed by us (106) with complete band gaps exceeding 29% for refractive index contrasts of 3.6 (106). This structure is amenable to fabrication with layer-by-layer methods.

Selected Applications of Photonic Crystals. Photonic crystals have been known to create cavities with defect modes within the photonic band gap. A planar Fabry-Perot type of cavity was created in the layer-by-layer crystal by separating the unit cells by a displacement d. The displacement d was adjusted to produce the defect mode within the band gap (107). A dipole antenna was placed within the cavity and driven at frequencies within the band gap. At the frequency of the defect mode an exceptionally directional pattern can emerge from the dipole antenna. Using an asymmetric cavity with different unit cells on the two sides we obtained (107) a source radiating in a forward di-

rection with a full width of 14° in the E-plane and 12° in the H-plane (Fig. 19).

It would be extremely difficult to obtain such an exceptionally directive source with conventional antenna array and we estimate >300 antennas in a phased array would be required to achieve such directionality. The simulated radiation pattern from the FDTD method agreed very well with the measurements performed on microwave-scale photonic crystals (107, 108). Very directional antennas have also been created by locating the antenna sources inside the photonic crystal and measuring the radiation emerging from the surface (109).

This work demonstrates that altering the densities of photonic states by a photonic crystal can drastically alter the emissive properties of sources, one of the original motivations for photonic crystals. Modifying the spontaneous emission of atomic sources by altering the photonic densities of states in 2-D and 3-D photonic crystals is an area of much activity.

Waveguides can easily be created in the layer-by-layer photonic crystal by removing an entire rod (X-waveguide), portions of a rod along the y-axis (Y-guide), or rod segments along the z-axis (Z-guide) (110). The X-waveguide has a wide band in the photonic band gap where the modes are transported. Waveguide bends are a novel application where EM waves can be turned through sharp bends without loss/scattering inherent in traditional waveguide geometries. Since the waveguide mode is confined within the bandgap, there is no loss to radiation modes in the bend region. We have carefully optimized the geometry of the bend to achieve near 100% bending efficiency and show (Fig. 23) the bending of a beam through 90° between two X-waveguides, simulated with the FDTD method. These simulations agree very well with measurements on microwave-scale photonic crystals(111, 112). Although such waveguide bends have been extensively investigated in 2-D photonic crystals for optical circuits, there can be significant loss in the z-direction at the bend region in the 2-D photonic crystals.

Another novel application is the add-drop filter using 3-D photonic crystals. In telecommunications applications using wavelength division multiplexing to carry dense streams of data, the input stream consists of various frequency channels. It is critical to select or drop one frequency from this stream to an output guide. Conversely it is also necessary to add a particular frequency channel to an in input stream. We have achieved such an add-drop filter with our 3-D photonic layer-by-layer photonic crystal. The configuration consists of an input and output waveguides which are separated by L and uncoupled (since L is several unit cells). There is a defect cavity located in a layer one unit cell above the waveguides that can support localized defect modes. When the input frequency matches the frequency of the defect that mode is excited in the defect cavity and transported to the output waveguide (113). Other waveguide modes are unaffected. Such 3-D add-drop filters can be an alternative to the extensively studied add-drop filters investigated with 2-D photonic crystals.

It is interesting to note that the concept of impedance which is critical to matching waveguides and has played a very important role in microwave engineering, can be de-

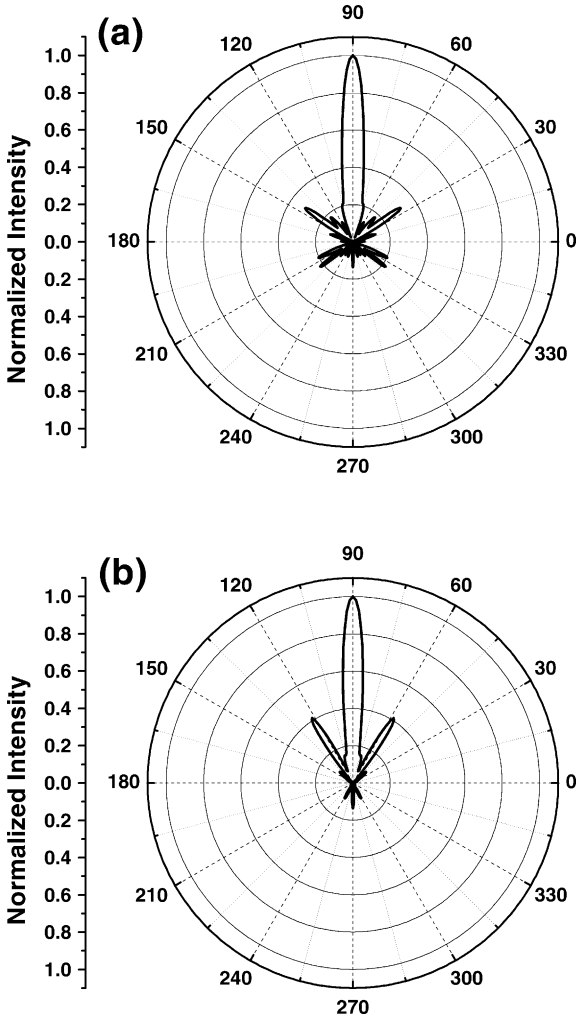

Figure 22. Radiation pattern in the (a) E-plane and the (b) H-plane for a dipole radiator placed inside an asymmetric cavity formed inside a photonic crystal. 2 unit cells are separated from 3 unit cells with this planar cavity.

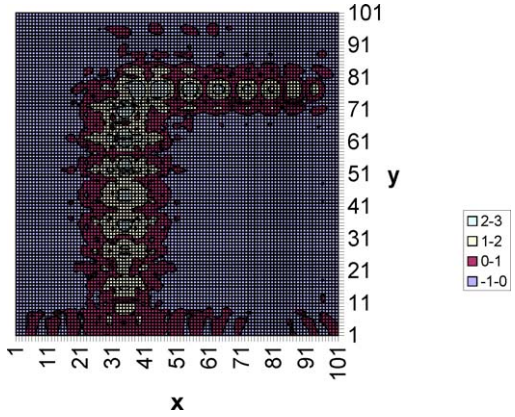

Figure 23. Bending of an electromagnetic wave around a 90 degree bend formed by two X-waveguides in the layer-by-layer photonic crystal, using FDTD simulation. The frequency is chosen to lie within the band gap of the photonic crystal.

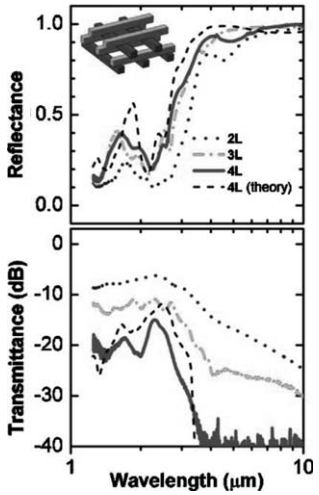

Figure 24. Measured reflection and transmission of the metallic layer-by-layer structure as a function of the number of layers, compared with simulations with the scattering matrix method.

fined analogously for photonic crystals as a ratio of the energy density to the power flow at each frequency (114). This impedance concept can account for reflection and transmission of waves from photonic crystals.

Metallic Photonic Crystals. Metallic photonic crystals have been an active subfield. As mentioned earlier the layer-by-layer photonic crystal has been fabricated with tungsten (58, 59) at rod separations from a=2−5 μ using advanced silicon processing methods (58, 59) or more recently with soft lithographic methods (97). The basic characteristic of the metallic layer-by-layer photonic crystal is that the reflectance is high (near 100%) and the transmission negligible at long wavelengths λ>a where the details of the structure are not resolved. At a wavelength $\lambda\sim$a the reflectance dips and the transmission increases (Fig. 24) for shorter wavelengths. There is an absorption peak located near the wavelength $\lambda\sim$a. Since the emission is the absorption modulated by the black-body emissivity, the thermal emissivity can be significantly altered and consists of an emission peak located near $\lambda\sim$a.

In contrast to connected metallic structures it is instructive to compare the case of isolated metallic scatterers. In this case the system is highly transmitting with little reflection for low frequencies upto a cutoff frequency defined by the lattice spacing. Above the cut-off frequency the transmission decreases with increase of reflection and absorption in the structure. An example of this behavior is the EM wave propagation in isolated metallic scatterers embedded in air [cermet topology (115, 116).

Figure 25 shows the transmission and absorption of EM waves propagating in simple cubic (*s.c.*) lattice consisting of metallic spheres with filling ratio $f = 0.03$. The system is infinite along the x and y directions, whereas its thickness along the z axis is $L = 4a$, and the incident waves with k along the z axis. The results for both polarizations are the same because of the lattice symmetry. For the present as well for all the following cases, each unit cell is divided into $10 \times 10 \times 10$ cells. Calculations with more subcells show that the convergence is better than 5% for the periodic cases, and better than 15% for the defect cases. There are two drops in the transmission (Fig. 25); the first around $va/c = 0.45$ and the second (and sharpest) one around 0.85. The wavevector k, parallel to the z axis corresponds to the $\Gamma - X$ direction in the k space. In this case, we expect the first gap to appear at the edge of the zone (in the X point) for va/c about 0.5, which is slightly higher than the frequency where the first drop in the transmission appears in this direction (Fig. 25). Because of the small filling ratio, there is no full band gap because the gaps in different directions do not overlap. We find similar results for fcc, bcc, and diamond structures with isolated metallic spheres or cubes. For the cases where the metal forms isolated scatterers, the results are similar to those of the dielectric PBG materials. The present results for the isolated metallic scatterers are in agreement with the results of a recent work (117) in which monolayers consisting of metallic spheres with radius between 10 and 100 nm were studied. The frequency-dependent Drude dielectric function (118) was used in these simulations

Perspectives and Future Directions. We briefly describe some applications of PBG materials on waveguides, light-emitting diodes, nonlinear effects, and quantum electrodynamics.

Recent studies of two-dimensional photonic band gap waveguides have shown encouraging results for the use of photonic crystals in order to improve waveguide efficiency (119, 120). In one of the studies (119), a two-dimensional square lattice consisting of dielectric cylinders was used. A line of cylinders was removed in order to create the waveguide geometry. Numerical simulations using the FDTD method revealed complete transmission at certain frequencies and very high transmission (>95%) over wide frequency ranges. High transmission is observed even for 90° bends with zero radius of curvature, with maximum transmission of 98% as opposed to 30% for analogous conventional dielectric waveguides. More studies, especially on 3-D structures, are needed. Also, measurements on similar systems are highly desirable.

In another interesting theoretical study (121), a thin slab of two-dimensional photonic crystal was shown to alter drastically the radiation pattern of spontaneous emission. By eliminating all guided modes at the transition frequencies, spontaneous emission can be coupled entirely to free space modes, resulting in a greatly enhanced extraction efficiency. Such structures might provide a solution to the long-standing problem of poor light extraction from high refractive-index semiconductors in light-emitting diodes (121). Extension of these studies into 3-D photonic crystals will be very useful. Two-dimensional photonic crystals have been combined with an array of holes in a metal sheet (49) to enhance the emission of infrared wavelengths from this structure.

There has been research on nonlinear photonic band gap materials, focused on 1-D photonic crystals (122–125). Under certain circumstances, there may be nonlinear wave propagation within the photonic band gap. For a large-scale photonic band gap material, the propagation of high intensity, nonlinear solitary waves may provide a practical way

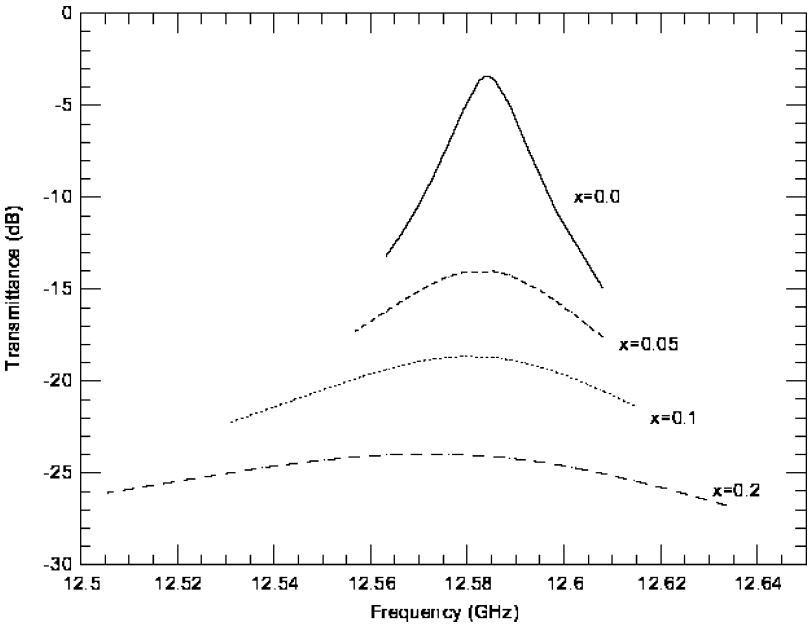

Figure 25. Transmission and absorption vs. the dimensionless frequency | ∗ nu ∗ |a/c for EM waves propagating in a 3-D s.c. lattice consisting of metallic spheres with f = 0.03, L = 4a, and | ∗ theta ∗ | = 0°. Solid and dotted lines correspond to a = 1.27 and 12.7 | ∗ nu ∗ |m, respectively.

of coupling large amounts of optical energy into, and out of, the otherwise impenetrable photonic band gap. A stationary solitary wave may be regarded as a self-localized state. In a perfectly periodic material, the high light-intensity itself creates a localized dielectric defect through the nonlinear Kerr coefficient. Unlike the localized state induced by static disorder, the localized dielectric defect is free to move with the light intensity field. The result is a solitary wave that can move through the bulk photonic band gap material with any velocity ranging from zero up to the average speed of light in the medium. Using a variational method, John and Akozbek (126) found a variety of different solitary wave solutions in two dimensions. Their work suggests that photonic band gap materials in higher dimensions may have a variety of interesting bistable switching properties that go beyond the simple characteristic of one-dimensional dielectrics. Because an exact solution is no longer possible in two and three dimensions, numerical methods are required to solve this problem. The FDTD method described earlier with implementation of the formalism described in 127 is very promising for the solution of this problem.

There are also very interesting implications of photonic crystals on quantum electrodynamics. For a single excited atom with transition frequency ω_o to the ground state, which lies within the band gap, there is no true spontaneous emission of light. A photon that is emitted by the atom finds itself within the classically forbidden energy gap of the photonic crystal. The result is a coupled eigenstate of the electronic degrees of freedom of the atom and the electromagnetic modes of the photonic crystal. This photon-atom bound state (128–130) is the optical analog of an electron-impurity level bound state in the gap of a semiconductor. When a collection of atoms is placed into the photonic crystal, a narrow photonic impurity band is formed within the larger photonic band gap. This may lead to new effects in nonlinear optics and laser physics (128).

Photonic crystals have created such a major revolution in manipulating electromagnetic waves that several new fields of active research have emerged from them. One of the most active subfields are meta-materials or left-handed materials. Another subfield is the area of sub-wavelength hole arrays. Left-handed materials can be realized by having ? and ? negative in a certain frequency range. Higher frequency bands on photonic crystals where the group velocity is opposite to the propagation k-vector are an example of left-handed behavior.

Sub-wavelength arrays of holes in metallic layers are another sub-field where metallic components with strong diffractive effects come into play. While many worldwide research groups have engineered very impressive 2-D photonic crystals, a goal of much present research is to fabricate three-dimensional photonic crystals at optical wavelengths and generate new applications to light-emitting devices and lasers.

ACKNOWLEDGMENTS

It is a pleasure to thank our colleagues C. T. Chan, E. Ozbay, W. Leung, K. Constant, J.H. Lee, and J. S. McCalmont for their insights and collaboration. We thank D. Crouch for providing FDTD simulations. This work was partially supported by the Director for Energy Research, Office of Basic Energy Sciences and Advanced Energy Projects. We also acknowledge support from the Department of Commerce through the Center for Advanced Technology (*CATD*). One of us (R.B) also acknowledges National Science Foundation funding through grants ECS-0601377 and DMR-0346508. The Ames Laboratory is operated for the U.S. Department of Energy by Iowa State University under Contract No. W-7405-Eng-82.

BIBLIOGRAPHY

1. Development and applications of materials exhibiting photonic band gaps, *J. Opt. Soc. Am. B* **10**: 1993(a special fea-

ture issue edited by C. M. Bowden, J. P. Dowling, and H. O. Everitt).

2. For a review seeC. M. Soukoulis (ed.), *Photonic Bandgaps and Localization*, New York: Plenum, 1993.
3. J. D. Joannopoulos R. D. Meade J. N. Minn *Photonic Crystals*, Princeton, NJ: Princeton University Press, 1995.
4. For a review seeC. M. Soukoulis, (ed.), *Photonic Band Gap Materials*, papers in *Proc. NATO Advanced Study Institute*, Kluwer, 1996.
5. E. Yablonovitch *Phys. Rev. Lett.*, **58**: 2059, 1987.
6. J. Martorell N. M. Lawandy *Phys. Rev. Lett.*, **66**: 887, 1991.
7. J. Martorell N. M. Lawandy *Phys. Rev. Lett.*, **65**: 1877, 1990.
8. B. Y. Tong *et al. J. Opt. Soc. Am. B*, **10**: 356, 1993.
9. S. John *Phys. Rev. Lett.*, **58**: 2486, 1987; S. John, *Comments Cond. Mat. Phys.*, **14**: 193, 1988.
10. A. Z. Genack N. Garcia *J. Opt. Soc. Am. B*, **10**: 408, 1993.
11. G. Kurizki A. Z. Genack *Phys. Rev. Lett.*, **66**: 1850, 1991.
12. S. John *Physics Today*, **44**: 32, 1991.
13. L. M. Brekhovskikh *Waves in Layered Media*, New York: Academic Press, 1960.
14. P. Yeh *Optical Waves in Layered Media*, New York: John Wiley & Sons, 1988.
15. A. Thelen *Design of Optical Interference Coatings*, New York: McGraw-Hill, 1989.
16. C. M. Bowden J. P. Dowling H. O. Everitt, (eds.) Development and applications of materials exhibiting photonic band gaps, *J. Opt. Soc. Am. B*, **10**: 1993.
17. E. Yablonovitch, Photonic crystals,. *J. Mod. Opt.*, **41**: 209, 1994.
18. E. Yablonovitch T. J. Gmitter *Phys. Rev. Lett.*, **63**: 1950, 1989.
19. K. M. Leung Y. F. Liu *Phys. Rev. Lett.*, **65**: 2646, 1990.
20. Z. Zhang S. Satpathy *Phys. Rev. Lett.*, **65**: 2650, 1990.
21. K. M. Ho C. T. Chan C. M. Soukoulis *Phys. Rev. Lett.*, **65**: 3152, 1990.
22. C. T. Chan K. M. Ho C. M. Soukoulis *Europhysics Lett.*, **16**: 563, 1991.
23. E. Yablonovitch T. J. Gmittner K. M. Leung *Phys. Rev. Lett.*, **67**: 2295, 1991.
24. K. M. Ho C.T. Chan, C.M. Soukoulis, R. Biswas, and M. Sigalas *Solid State Commun.*, **89**: 413, 1994.
25. E. Ozbay *et al. Phys. Rev. B*, **50**: 1945, 1994.
26. E. Ozbay *et al. Appl. Phys. Lett.*, **64**: 2059, 1994.
27. E. Ozbay *et al. Optics Lett.*, **19**: 1155, 1994.
28. E. Ozbay *et al. Appl. Phys. Lett.*, **65**: 1617, 1994.
29. E. Ozbay *et al. Appl. Phys. Lett.*, **67**: 1969, 1995.
30. E. Ozbay *et al. Phys. Rev. B*, **51**: 13961, 1995.
31. M. C. Wanke *et al. Science*, **275**: 1284, 1997.
32. E. Yablonovitch *et al. Phys. Rev. Lett.*, **67**: 3380, 1991.
33. R. D. Meade *et al. Phys. Rev. B*, **44**: 13772, 1991.
34. R. D. Meade *et al. Phys. Rev. B*, **48**: 8434, 1993.
35. S. Satpathy Z. Zhang M. R. Salehpour *Phys. Rev. Lett.*, **64**: 1239, 1990.
36. R. Biswas *et al.* Photonic band gap materials, *Proc. NATO Advanced Study Institute* 315, Kluwer, 1995, p. 23.
37. J. B. Pendry A. MacKinnon *Phys. Rev. Lett.***69**: 2772, 1992; J. B. Pendry, *J. Mod. Opt.*, **41**: 209, 1994.
38. M. M. Sigalas *et al. Phys. Rev. B*, **48**: 14121, 1993.
39. M. M. Sigalas *et al. Phys. Rev. B*, **49**: 11080, 1994.
40. M. M. Sigalas *et al. Phys. Rev. B*, **52**: 11744, 1995.
41. J. S. McCalmont *et al. Appl. Phys. Lett.*, **68**: 2759, 1996.
42. M. M. Sigalas *et al. Appl. Phys. Lett.*, **68**: 3525, 1996.
43. K. S. Yee *IEEE Trans. Antennas Propag.* **14**: 302, 1966.
44. K. Kunz R. Luebbers *The Finite Difference Time Domain Method for Electromagnetics*, Boca Raton, FL: CRC Press, 1993.
45. K. Umashankar A. Taflove *Computational Electromagnetics*, Boston: Artech House, 1993.
46. M. M. Sigalas R. Biswas *et al. Microw. Opt. Technol. Lett.*, **15**: 153, 1997.
47. Z.Y. Li L. L. Lin *Phys. Rev. E*, **67**: 046607, (2003) .
48. L. L. Lin Z.Y. Li and K.M. Ho *J. Appl. Phys.*, **94**: 811, (2003) .
49. R. Biswas, C.G. Ding, I. Puscasu, M. Pralle, M. McNeal, J. Daly, A. Greenwald, E. Johnson, *Phys. Rev. B.*, **74**, 045107 (2006) .
50. L. Li, *J. Opt. Soc. Am.* **13**, 1024 (1996) .
51. E. Yablonovitch. *Scientific American*(International Edition), **285**,no. 6,pp. 47–55, (2001) .
52. K. Sakoda, *Optical properties of photonic crystals*, Springer-Verlag(Berlin-Heidelberg) (2005) .
53. S. Lin, J.G. Fleming, D.L. Hetherington, B.K. Smith, R. Biswas, K.-M. Ho, M.M. Sigalas, W. Zubrzycki, S.R. Kurtz, and J. Bur, *Nature* **394**, 251 (1998) .
54. J. G. Fleming and S. Y. Lin, *Opt. Lett.* **24**, 49 (1999) .
55. S. Noda, K. Tomoda, N. Yamamoto, A. Chutinan, *Science* **289**, 604 (2000) .
56. G. Subramania and S. Y. Lin,*Appl. Phys. Lett.* **85**, 5037 (2004) .
57. Fleming, S. Lin, I. El-Kady, R. Biswas, and K. M. Ho, *Nature* **417**, 52–55 (2002) .
58. C.H. Seager, M.B. . . Sinclair, J. Fleming. *Appl. Phys. Lett* **86**, 244105 (2006) .
59. T. F. Krauss R. M. De La Rue S. Brand *Nature*, **383**,: 699, 1997.
60. J. O'Brien *et al. Electronic Lett.*, **32**: 2243, 1996.
61. M. Kanskar *et al. Appl. Phys. Lett.*, **70**: 1438, 1997.
62. V. Berger O. Gauthier-Lafaye E. Costard *Electronic Lett.* **33**: 425, 1997.
63. P. W. Evans J. J. Wierer N. Holonyak Jr. *Appl. Phys. Lett.*, **70**: 1119, 1997.
64. U. Gruning V. LehmannInC. M. Soukoulis, (ed.), *Photonic Band Gap Materials*, Dordrecht: Kluwer, 1996, p. 453.
65. U. Gruning V. Lehmann C. M. Engelhardt, *Appl. Phys Lett* **66**, 3254 (1995) .
66. S. M. Weiss, M. Molinari, and P. M. Fauchet C. C. Striemer and P. M. Fauchet, *Appl. Phys. Lett* **83**, 1980 (2003) .
67. C.C. Cheng. A. Scherer, V. Arbet-Engels, E. Yablonovitch, *J. VAc. Science and Technology* **14**, 4110 (1996) .
68. G. Feiertag *et al. Photonic Band Gap Materials*, Dordrecht: Kluwer, 1996, p. 63; G. Feirtag *et al.*, *Appl. Phys. Lett.* **71**: 1441, 1997.
69. Koichi Awazu *et al* J. Vac. *Sci. Technol. B* **23**, 934 (2005) .
70. O. Toader M. Berciu and S. John, *Phys. Rev. Lett.* **90**, 233901 (2003) .
71. M. Campbell, D. N. Sharp, M. T. Harrison, R. G. Denning, and A. J. Turberfield, *Nature*(London) **404**,53 (2000) .
72. Yu. V. Miklyaev, D. C. Meisel, A. Blanco, G. von Freymann, K. Busch, W. Koch, C. Enkrich, M. Deubel, and M. Wegener, *Appl. Phys. Lett.* **82**, 1284 (2003) .

73. D. Meisel, M. Wegener, K. Busch, *Phys. Rev B* **70**, 165104 (2004) .
74. M. Deubel, G. von Freymann, M. Wegener, S. Pereira, K. Busch, and C. M. Soukoulis, *Nature. Mater.* **3**, 444 (2004) .
75. O. Toader, T. Y. M. Chan, and S. John, *Appl. Phys. Lett.* **89**, 101117 (2006) .
76. J.W. Rinne and P. Wiltzius, *Opt. Express* **14**, 9909 (2006) .
77. R. Biswas, M. Sigalas, G. Subramania, and K.-M. Ho, *Phys. Rev. B* **57**, 3701 (1998) .
78. K. Busch and S. John, *Phys. Rev. E* **58**, 3896 (1998) .
79. R. Biswas, M. Sigalas, G. Subramania, C.M. Soukoulis, K.M. Ho, *Phys. Rev. B* **61**, 4549 (2000) .
80. J.E.G. Wijnhoven and W.L. Vos, *Science* **281**, 802 (1998) .
81. B.T. Holland, C.F. Blanford, and A. Stein, *Science* **281**, 538 (1998) .
82. A. Imhof and D.J. Pine, *Nature*∼London **389**, 448 (1997) .
83. A. Velev, T.A. Jede, R.F. Lobo,and A.M. Lenhoff, *Nature*(London) **389**, 448 (1997) .
84. A. Zakhidov *et al.*, *Science* **282**, 897 (1998) .
85. Y. A. Vlasov, X-Z. Bo, J. G. Strum, and D. J. Norris, *Nature* **414**, 289 (2000) .
86. Rajesh Rengarajan, Peng Jiang, Diane C. Larrabee, Vicki L. Colvin, and Daniel M. Mittleman, *Phys. Rev. B* **64**, 205103 (2001) .
87. A. Blanco, E. Chomski, S. Grabtchak, M. lbisate, S. John, S. W. Leonard, C. Lo′pez, F. Meseguer, H. Mi′guez, J. P. Mondia, G. A. Ozin, O. Toader, and H. M. van Driel, *Nature*(London) **405**, 437 (2000) .
88. G. Subramania, K. Constant, R. Biswas, M.M. Sigalas, and K.-M. Ho, *Appl. Phys. Lett.* **74**, 3933 (1999) .
89. G. Subramania, K. Constant, R. Biswas, M.M. Sigalas, K.-M. Ho, *Phys. Rev. B.* **63**, 235111 (2001) .
90. V. N. Astratov *et al. Phys. Lett. A*, **222**: 349, 1996.
91. V. N. Bogomolov *et al. Applied Phys. A*, **63**: 613, 1996.
92. R. D. Pradhan J. A. Bloodgood G. H. Watson *Phys. Rev. B*, **55**: 9503, 1997.
93. R. Mayoral *et al. Advanced Materials*, **9**: 257, 1997.
94. F. Garcı́a-Santamarı́a, C. López, and F. Meseguer *et al*, *Appl. Phys. Lett.* **79**, 2309 (2001) .
95. Kanna Aoki, Hideki T. Miyazaki, Hideki Hirayama, Kyoji Inoshita, Toshihiko Baba, Norio Shinya, and Yoshinobu Aoyagi, *Appl. Phys. Lett.* **81**, 3122 (2002) .
96. W. Y. Leung, H. Kang, K. Constant, D. Cann, C.-H. Kim, R. Biswas, M. M. Sigalas, and K.-M. Ho, *J. Appl. Phys.* **93**, 5866 (2003) .
97. Jae-Hwang Lee, Chang-Hwan Kim, Yong-Sung Kim, and Kai-Ming Ho, K. Constant, and C.H. Oh, *Appl. Phys. Lett.* **88**, 181112 (2006) .
98. R. Biswas J. Ahn, T. Lee, J.-H. Lee, Y.S. Kim, C.H. Kim, C.H. Oh, W. Leung, K. Constant, K.-M. Ho, J. Optical *Society of America B* **22**, 2728 (2005) .
99. Shinpei Ogawa, Masahiro Imada, Susumu Yoshimoto, Makoto Okano, Susumu Noda, *Science* **305**, 227 (2003) .
100. Takashi Asano, Bong-Shik Song, and Susumu Noda, Optics Express **14**, 1996 (2006) .
101. Hitomichi Takano, Bong-Shik Song, Takashi Asano, and Susumu Noda, *Appl. Phys. Lett* **86**, 241101 (2005) .
102. R. Biswas, M. Sigalas, K.M. Ho, and S. Lin, *Phys. Rev. B.* **65** 205121 (2002) .
103. S. Lin, P. Fleming, M.M. Sigalas, R. Biswas, and K.-M. Ho, J. Optical *Society of America B.* **18**, 32 (2001) .
104. S. G. Johnson and J. D. Joannopoulos, *Appl. Phys. Lett.* **77**, 3490 (2000) .
105. D. Roundy, J. D. Joannopoulos, *Appl. Phys. Lett.* **82**, 3835 (2003) .
106. R. Biswas, I. El-Kady, and K.-M. Ho, *Photonics and Nanostructures* **1**, 15 (2003) .
107. R. Biswas, E. Ozbay, B. Temelkuran, M. Bayindir, M.M. Sigalas, and K-M. Ho, J. Optical *Society of America B.* **18**, 1684 (2001) .
108. B. Temelkuran, M. Bayindir, E. Ozbay, R. Biswas, G. Tuttle, M.M. Sigalas, and K-M. Ho, *Journal of Applied Physics* **87**, 603 (2000) .
109. I. Bulu, H. Caglayan, E. Ozbay, *Appl. Phys. Lett.* **83**, 2363 (2003) .
110. C. Sell, C. Christensen, J. Muehlmeier, G. Tuttle, Z.Y. Li, and K.M. Ho, *Applied Physics, Letters* **83**, 4605 (2004) .
111. M. Bayindir, E. Ozbay, B. Temelkuran, M. M. Sigalas, C. M. Soukoulis, R. Biswas, K. M. Ho, *Phys. Rev. B* **63**, 081107(R) (2001) .
112. S. Noda, N. Yamamoto, H. Kobayashi, M. Okano, and K. Tomoda, *Appl. Phys. Lett.* **75**, 904 (1999) .
113. P Kohli, C. Christensen, J. Muehlmeier, R. Biswas, G. Tuttle, and K.-M. Ho, *Appl. Phys. Lett.* **89**, 231103 (2006) .
114. R. Biswas, Z.-Y. Li and K. M. Ho, Applied Physics *Letters*. **84**, (8) 1254 (2004) .
115. W. Lamb D. M. Wood N. W. Ashcroft *Phys. Rev. B*, **21**: 2248, 1980.
116. E. N. Economou M. M. Sigalas *Phys. Rev. B*, **48**: 13434, 1993.
117. N. Stefanou A. Modinos *J. Phys. Condens. Matter*, **3**: 8135, 1991.
118. J. D. Jackson *Classical Electrodynamics*, New York: Wiley, 1975.
119. A. Mekis *et al. Phys. Rev. Lett.*, **77**: 3787, 1996.
120. J. G. Maloney *et al. Microw. Opt. Technol. Lett.*, **14**: 261, 1997.
121. S. Fan *et al. Phys. Rev. Lett.*, **78**: 3294, 1997.
122. M. D. Tocci *et al. Appl. Phys. Lett.*, **66**: 2324, 1995.
123. E. Lidorikis Q. Li C. M. Soukoulis *Phys. Rev. B*, **54**: 10249, 1996; E. Lidorikis *et al.*, *Phys. Rev. B*, **56**: 15090, 1997.
124. T. Hattori N. Tsurumachi H. Nakatsuka *J. Opt. Soc. Am.*, **14**: 348, 1997.
125. R. Wang J. Dong D. Y. Xing *Phys. Rev. E*, **55**: 6301, 1997.
126. S. John N. Akozbek *Phys. Rev. Lett.*, **71**: 1168, 1993.
127. R. W. Ziolkowski J. B. Judkins *J. Opt. Soc. Am. B*, **10**: 186, 1993.
128. S. John J. Wang *Phys. Rev. B*, **43**: 12772, 1991; S. John, and T. Quang *Phys. Rev. A*, **50**: 1764, 1994.
129. S. Bay P. Lambropoulos K. Molmer *Opt. Commun.*, **132**: 257, 1996.
130. A. Kamli *et al. Phys. Rev. A*, **55**: 1454, 1997.

M. M. SIGALAS
K. M. HO
C. M. SOUKOULIS
R. BISWAS
G. TUTTLE

Ames Laboratory-U.S. DOE and Department of Physics and Astronomy, Ames, IA, 50011
Ames Laboratory-U.S. DOE, Department of Physics and Astronomy, Microelectronics Research Center, Ames, IA, 50011
Microelectronics Research Center, Department of Electrical and Computer Engineering, Ames, IA, 50011